UNIVERSITÉ DU QUÉBEC À MONTRÉAL

L'APPROCHE METHODOLOGIQUE À LA VALIDATION D'UNE PARAMETRISATION DES AÉROSOLS ET NUAGES EN UTILISANT LE SIMULATEUR DES INSTRUMENTS D'EARTHCARE

MÉMOIRE
PRÉSENTÉ
COMME EXIGENCE PARTIELLE
DE LA MAÎTRISE EN SCIENCES DE L'ATMOSPHÈRE

PAR
ALEKSANDRA TATAREVIC

AVRIL 2009

UNIVERSITÉ DU QUÉBEC À MONTRÉAL

METHODOLOGICAL APPROACH TO THE VALIDATION OF THE AEROSOL-CLOUD PARAMETERIZATION USING THE EARTHCARE INSTRUMENT SIMULATOR

THESIS
PRESENTED
IN PARTIAL FULLFILMENT
OF THE REQUIREMENTS FOR THE MASTER'S DEGREE
IN ATMOPSHERIC SCIENCES

BY
ALEKSANDRA TATAREVIC

APRIL 2009

REMERCIEMENTS

Je tiens à adresser mes remerciements les plus sincères à mon directeur, Dr. Jean-Pierre Blanchet, qui m'a donné l'opportunité de réaliser ce projet. Sa rigueur scientifique, ses judicieux conseils, sa disponibilité et son enthousiasme soutenu dans ce projet ont grandement contribué à finaliser ce travail. Je tiens également à le remercier du soutien financier qu'il m'a offert tout le long de ma maîtrise, et aussi pour la chance de pouvoir continuer cette recherche.

Je désire aussi adresser des remerciements particuliers à Dr. Eric Girard pour tous ses conseils et ses encouragements tout au long de ce projet.

Je veux remercier aussi mes collègues avec lesquels j'ai collaboré et qui m'ont aidé à finaliser divers travaux pendant ma maîtrise. Un grand merci à ma famille qui m'a encouragée et donné le soutien moral.

Je remercie finalement tous ceux qui m'ont manifestés de la bonne volonté pendant la durée de mon projet.

CONTENTS

LIST OF FIGURES

LIST OF TABLES

LIST OF ACRONYMS, ABBREVIATIONS AND SIGLA

ACE-Asia	Asian Pacific Regional Aerosol Characterization Experiment
AOPM	Aerosol Optical Parameters Module
APEX	Asian Atmospheric Particle Change Studies
ATLID	Atmospheric Lidar
BBR	Broadband Radiometer
CALIPSO	Cloud-Aerosol Lidar and Infrared Pathfinder Satellite Observations
CAM	Canadian Aerosol Module
CAM-CCC GCM III	Canadian Aerosol Module - Third Generation Canadian Climate Centre General Circulation Model
CCN	Cloud condensation nucleus
CLARE	Cloud Lidar And Radar Experiment
CPR	Cloud Profiling Radar
CRCM	Canadian Regional Climate Model
CRYSTAL-FACE	Cirrus Regional Study of Tropical Anvils and Cirrus Layers-Florida Area Cirrus Experiment
Empirical IWC-RRF	Radar reflectivity profiles computed from NARCM ice water content via empirical relations between NARCM IWC and RRF
Empirical LWC-RRF	Radar reflectivity profiles computed from NARCM liquid water content via empirical relations between NARCM LWC and RRF
EarthCARE	Earth Clouds Aerosol and Radiation Explorer
EC-IWC-RRF	Simulated radar reflectivity profiles from NARCM ice water content via EarthCARE Instrument Simulator
EC-LWC-RRF	Simulated radar reflectivity profiles from NARCM liquid water content via EarthCARE Instrument Simulator

ECMWF	European Centre for Medium Range Weather Forecasting
ESA	European Space Agency
FOV	Field-Of-View
GCCM	General Circulation Climate Model
GMT	Greenwich Mean Time
G2	Gulfstream-2
HSR	High-Spectral-Resolution
IN	Ice nuclei
INDOEX	Indian Ocean Experiment
IS	Instrument Simulator
IWC	Ice water content
IWC-RRF	Radar reflectivity profiles computed from NARCM ice water content by utilizing modified-gamma distribution
JAXA	Japanese Aerospace Exploration Agency
JST	Japan Standard Time
Lidar	Light Detection And Ranging
LITE	Lidar In-space Technology Experiment
LWC	Liquid water content
LWC-RRF	Radar reflectivity profiles computed from NARCM liquid water content by utilizing modified-gamma distribution
MSI	Multi-Spectral Imager
Nd:YAG	Neodymium: Yttrium Aluminum Garnet
NARCM	Northern Aerosol Regional Climate Model
NASA	National Aeronautics and Space Administration
NICT	National Institute of Communication Technology

OPAC	Optical Properties of Aerosol and Clouds
Radar	Radio Detection And Ranging
RF	Relative Frequency
RRF	Radar reflectivity factor
SNR	Signal-to-noise-ratio
STS	Space Transportation System
UFF	Universal File Format
UV	Ultraviolet
3-D	Three-dimensional

LIST OF SYMBOLS, VARIABLES AND PARAMETRES

a	aerosol bin radius (μm)
c	speed of light (ms^{-1})
c_o	dimensionless parameter in the linear relation between the effective radius and the mean volume radius used in Johnson (1993) parameterization
c_1, c_2	dimensionless parameters used in empirical relationship between the effective radius and the ice water content, used by Lohmann and Roeckner (1996)
C_{lid}	lidar instrument constant
C_{rad}	radar instrument constant
D	diameter of cloud particle (m)
D_{eq}	equivalent melted diameter of the particle (m)
f	frequency (GHz in radar applications and m^{-1} in the case of lidar)
h	height (m)
i	aerosol size bin (μm)
k	size parameter (m^{-1})
K	dimensionless factor incorporating the refractive index of the scattering cloud particles
K_h	attenuation coefficient due by hydrometeors ($dBZkm^{-1}$)
K_t	total attenuation coefficient due by gases and hydrometeors ($dBZkm^{-1}$)
K_v	attenuation coefficient due by water vapour ($dBZkm^{-1}$)
$\lvert K_{W,3Ghz} \rvert^2$	dielectric factor for water and at wavelength of 3 GHz (dimensionless)
$\lvert K_{W,94Ghz} \rvert^2$	dielectric factor for water and at wavelength of 94 GHz (dimensionless)
m_{sulf}	sulphate aerosol mass (μgm^{-3})
n	number of hydrometeors of a given category per cubic meter and per interval of diameter ($m^{-3}\mu m^{-1}$)
$n(D)dD$	number of particles having a diameter in the radius interval D-$dD/2$, D+$dD/2$ and in unit of volume of the air (m^{-3})

N_0	total number concentration of particles per unit volume of air (m^{-3})
N_{dec}	number of photons arriving at lidar detector channel
N_i	number of samples
N_l	cloud droplet number concentration (m^{-3})
N_l^{cont}	cloud droplet number concentration for continental clouds (m^{-3})
N_l^{mor}	cloud droplet number concentration for maritime clouds (m^{-3})
p	pressure (Pa)
P_{back}	mean background power (Wm^{-2})
P_r	mean received power (Wm^{-2})
$P_{11}, P_{12}, P_{33}, P_{34}$	elements of Mie scattering matrix
$P(\pi)$	phase function for the scattering angle $\theta=\pi$
q_{ci}	cloud ice water content (kgm^{-3})
q_{cl}	cloud liquid water content (kgm^{-3})
r_e	equivalent volume (radius) of the liquid (ice) particle in the modified-gamma distribution
r_v	mean volume cloud droplet radius (m)
R	distance between instrument detector system and scattering object under consideration (m)
RRF	radar reflectivity factor (dBz)
S	lidar ratio ($srad$)
SD_k	standard deviation vertical profile of a random variable $\xi_{k,i}$
SSA	single scattering albedo (dimensionless)
$S_1(\theta), S_2(\theta)$	scattering functions in function of the scattering angle θ
tr	aerosol component (tracer)
T	temperature (K)
T_0	absolute temperature (K)
V	dry particle volume (m^3)
z_k	altitude level (m)
Z	radar reflectivity factor (dBZ or mm^6m^{-3})
Z_a	attenuated radar reflectivity factor ($dBZkm^{-1}$ or mm^6m^{-3})
Z_e	equivalent radar reflectivity (dBZ or mm^6m^{-3})

Z_M	apparent or measured radar reflectivity factor (dBZ or mm^6m^{-3})
β_e	extinction coefficient (m^{-1})
β_π	backscattering coefficient ($srad^{-1}m^{-1}$)
β_π^A	attenuated backscattering coefficient ($srad^{-1}m^{-1}$)
β_s	scattering coefficient (m^{-1})
Δt	time interval (s)
Δz_k	thickness of the model layer (m)
Γ	Gamma function
γ	dimensionless constant that defines the shape of the modified-gamma distribution
κ	Planck's constant ($6{,}626069\times10^{-34}\ m^2kgs^{-1}$)
λ	wavelength (m)
θ	scattering angle ($srad$)
ρ	dry aerosol density (kgm^{-3})
ρ_i	density of ice (kgm^{-3})
ρ_v	density of water vapour (kgm^{-3})
ρ_w	density of water (kgm^{-3})
ς	function of pressure, temperature and density in expression of Ulaby formulation for attenuation due to the water vapour
$\sigma_b(D)$	backscattering cross-section for droplets of diameter D (m^2)
σ_e	aerosol extinction wet-volume cross-section (m^2)
σ_π	aerosol backscattering wet-volume cross-section (m^2)
σ_s	aerosol scattering wet-volume cross-section (m^2)
τ	optical depth (dimensionless)
ξ	droplet volume (diameter) for liquid (solid) hydrometeors in modified-gamma distribution
$\bar{\xi}$	volume (size) of the liquid (solid) particle having the mean mass (mean radius) in modified-gamma distribution
$\xi_{k,i}$	random variable with subscripts k and i denoting vertical and horizontal level, respectively
$\bar{\xi}_k$	mean vertical profile of a random variable $\xi_{k,i}$

ξ_m	modified-gamma distribution characteristic size of a hydrometeor category
ζ	aerosol mass density (kgm^{-3})
$\sin\theta\, d\theta\, d\Phi$	scattering solid angle differential expressed in polar coordinates with θ being the polar angle and Φ being the azimuthal angle

RESUMÉ

La validation d'un modèle atmosphérique avec les observations satellitaires est basée sur les différentes techniques de télédétection employées afin de récupérer des propriétés physiques et optiques de composantes atmosphériques, notamment des nuages et des aérosols. Il est bien connu que le « retrieval approach » introduit de grandes incohérences en raison des hypothèses diverses portant sur le problème d'inversion où la principale difficulté est l'unicité de la solution. Autrement dit, le milieu analysé peut être composé d'un certain nombre de paramètres physiques inconnus dont les combinaisons différentes mènent au même signal de radiation. En plus du problème d'unicité de la solution, il y a plusieurs problèmes mathématiques reliés à l'existence et à la stabilité de la solution ainsi qu'à la manière dont la solution est construite. Par contre, il est bien connu que les prévisions des modèles atmosphériques souffrent d'incertitudes portant sur l'approche numérique qui limite leurs applications à la simulation de phénomènes naturels.

Malgré ces difficultés, certains aspects des prévisions numériques peuvent être considérées comme réalistes parce qu'elles prennent explicitement en considération les principes de la physique, dont des processus microphysiques des nuages et des aérosols. Dans ce contexte, la motivation principale de cette recherche est d'évaluer le potentiel de la validation des paramétrisations physiques des aérosols et des nuages dans les modèles climatiques par le biais des mesures satellitaires (radar et lidar) en utilisant les « simulation vers l'avant ».

Dans cette étude, nous utilisons une approche qui emploie le modèle *Simulateur des Instruments d'EarthCARE* afin de reproduire des mesures satellitaires comparables à celles du radar et du lidar. Compte tenu du manque de mesures satellitaires, la validation se base sur les mesures directes du lidar et du radar de l'expérience APEX-E3 réalisées au printemps 2003 où les fréquences et la performance des systèmes d'observation correspondent à celles qui vont être mesurées par le satellite EarthCARE. Les caractéristiques microphysiques des nuages et des aérosols ainsi que l'état de l'atmosphère sont produites par le modèle atmosphérique NARCM. Elles sont ensuite converties en données de réflectivité pour le radar et en données de rétrodiffusion pour lidar en utilisant le Simulateur des Instruments d'EarthCARE. Pour terminer, les résultats sont comparés aux mesures de radar et de lidar de l'expérience APEX-E3.

Les champs d'aérosols simulés avec NARCM indiquent un accord important avec ceux qui sont observés, mais les propriétés microphysiques des nuages simulées ne sont pas compatibles avec les observations. Autrement dit, les résultats montrent un large désaccord entre la réflectivité observée et la réflectivité simulée en dépit du fait que ses étendues verticales sont relativement similaires. Le nuage simulé est plus mince, situé à plus haute altitude et les valeurs maximales de réflectivité dans le nuage sont environ 5-10 *dBZ* inférieures à celles du nuage observé. De plus, le coefficient de la rétrodiffusion simulé (sans eau liquide) au-dessous de la base et au-dessus du sommet du nuage est nettement plus faible par rapport au coefficient de rétrodiffusion observé. Il y a également, à ces deux niveaux une plus grande quantité d'eau glacée observée que dans le cas simulé par NARCM. Si la

présence d'eau liquide est incluse dans le *Simulateur des Instruments d'EarthCARE*, les valeurs simulées du coefficient de rétrodiffusion sont de plusieurs ordres de grandeurs supérieures à celles observées, ce qui suggère que les valeurs du contenu en eau liquide simulées par NARCM sont surestimées d'une manière significative par rapport à toutes les altitudes où le nuage observé est présent.

En conclusion, l'analyse montre que la paramétrisation microphysique de Lohmann (Lohmann et Roeckner, 1996) ne possède pas la capacité de produire les quantités glace observées dans le cas de cirrostratus. Il est également constaté que le contenu d'eau glacé de NARCM est sous-estimé, et que le contenu d'eau liquide est surestimé. Les résultats de cette étude confirment donc que l'utilisation du « forward approach » a un grand potentiel dans la validation de la paramétrisation des aérosols et des nuages. Par contre, des nouvelles vérifications seront nécessaires pour accomplir le processus de validation.

Mots-clés: la validation, rétrodiffusion de lidar, la réflectivité de radar, les simulations régionales des modèles atmosphériques

ABSTRACT

Validation of atmospheric model by space-borne retrieval products introduces the considerable inconsistency because of variety of assumptions related to the inversion problem. Each retrieval approach assumes some information about shape, size distribution or composition, which can significantly impact retrieved microphysical properties. Meanwhile, it is well known that numerical uncertainties in atmospheric models may limit the accuracy of simulations of both the mean climate and its variability. On the other hand, model simulations can consider explicitly the fundamental physical and cloud (aerosol) microphysical processes. In this context, another way to validate an atmospheric model is to apply the *forward* approach, in which the atmospheric model provides the atmospheric state and the cloud and aerosol microphysical properties used to simulate the remotely sensed observations. In this context, the prime motivation of this research is to explore a general method of validating aerosol and cloud parameterization in climate models.

In this study, the EarthCARE Instrument Simulator (EarthCARE IS) is used as the forward model simulating measurements of space-borne radar and lidar instruments on an atmosphere generated by the Northern Aerosol Regional Climate Model (NARCM). In the absence of the space-borne EarthCARE measurements, this method is demonstrated using the Asian Atmospheric Particle Change Studies Experiment (APEX-E3) observations in East-Asia region during spring 2003. The frequencies as well as the performance of the APEX-E3 observing system correspond to those of the forthcoming EarthCARE-satellite measurements. The microphysical characteristics of the NARCM-simulated clouds and aerosol are converted into radar reflectivity factor and lidar backscattering using the EarthCARE IS and compared against the APEX-E3 airborne radar and lidar measurements.

Simulated aerosol fields show significant agreement with ones observed, but simulated cloud properties are not consistent with the observations. Results show a large discrepancy between the modelled and the observed reflectivity. Simulated clouds are thinner and located at higher altitudes than compared to observed clouds. The maximal values of simulated reflectivity underestimate observations by about 5-10 *dBZ*. Despite the considerable similarity in shape and vertical extent, the simulated backscatter, in the simulation with only ice water content, is significantly lower than the observed one, mostly below the base and above the top of simulated cloud. It is found that at those vertical levels observed ice water content is larger than that simulated by NARCM. If the presence of water droplets is included, values of the simulated backscatter coefficient would over-estimate observations by several orders of magnitude. Hence, it is found that the NARCM liquid water content may be significantly overestimated at all altitudes of the observed clouds. Further analysis shows that the Lohmann (Lohmann and Roeckner, 1996) microphysical scheme does not have the ability to produce an amount of ice water in the case of observed cirrostratus. Furthermore, it is found that NARCM underestimates ice water content and likely overestimates liquid water content.

The results of this study have confirmed that utilising the forward approach has a great potential for validation of aerosol and cloud parameterization in climate models. Testing the method, this study leads to its application in more extensive diagnostic for verifications for all clouds and aerosol types against a corresponding real atmosphere.

Keywords: forward validation approach, lidar backscatter, radar reflectivity, regional atmospheric model simulations

INTRODUCTION

The major source of uncertainty in climate models is the difficulty of representing clouds and aerosol and their interactions with radiation. Atmospheric aerosols have a crucial role in determining the Earth radiation balance via scattering and absorbing both solar and thermal radiation (direct climate effect) as well as through their role in forming and interacting with clouds (indirect effect). Accurate parameterisations of the indirect aerosol effects represent one of the most important issues in climate modelling. However, until recently, there has been no dataset that would provide global information on three-dimensional cloud and aerosol spatiotemporal distributions and their optical properties. Such a dataset would significantly improve our predictive capabilities of the climate system by improving current understanding of the Earth's radiation budget. It would also be crucial for the validation of climate models and the improvement of existing parameterisations of physical processes related to clouds, aerosol and radiative transfer in the atmosphere.

Observations from airborne campaigns and ground-based active and passive sensors at isolated sites are of very limited spatial and temporal resolution. They are best suited to investigating detailed microphysics in or near a cloud system. On the other hand, they are limited in providing a sufficiently large database for climate parameterisation. In this context, they cannot capture adequately the seasonal variability of cloud and aerosol nor the anthropogenic climate forcing through various human agricultural and industrial activities. On the other hand, satellite remote sensing holds the advantage of sounding the vertical structure of atmosphere. It offers a global picture of vertical profiles of cloud and aerosol properties with high spatial resolution. As such, satellite remote sensing is becoming an essential tool in monitoring the geographical and temporal coverage of clouds and aerosol required for initialisation and validation of atmospheric models.

Various remote sensing techniques are employed to retrieve physical and optical properties of the atmosphere that are essential to validate atmospheric models. Many studies (Evans and Stephens, 1995; Evans *et al.*, 1998) indicate that the active observing systems operating at millimetre (*mm*) and sub-*mm* wavelengths (radars) are the most suitable way for

monitoring the bulk properties of thicker clouds. Ice cloud effectively scatters radiation at *mm* wavelengths. This is the principal mechanism for the interpretation of the radar (Radio Detection And Ranging) signal. The attenuation of the radar signal by ice particles is small at 94 *GHz*. But, it is significant in the case of warm clouds and melting ice (Hogan and Illingworth, 1999).

The lidar (Light Detection And Ranging) technique is based also on the detection and analysis of backscattered lights, but at much short wavelengths. It results from the interactions of a laser beam with atmospheric constituents, both molecular and particulate. The key difference between lidar and cloud radar is that they operate at wavelengths that differ by about three orders of magnitude. Radar operates at microwave frequencies while lidar operates in the visible or infrared ranges. Lidar remains best suited for sounding of atmospheric aerosol (Franke *et al.*, 2001; Sassen, 2002) and optically thin clouds.

Lidar and radar have been used as ground-based, airborne and satellite-based instruments. They are providing high-resolution sampling of aerosol and cloud vertical profiles. Differences in the lidar and radar measurements are influenced by particle size. Radar is highly sensitive to large particles (raindrops, snowflakes, ice crystals, hailstones etc.) and can pass through dense convective layers. On the other hand, lidar is more sensitive to small cloud and aerosol particles, but cannot penetrate through optically thick clouds (McGill *et al.*, 2004). The lidar technique is very powerful to characterise the evolution and distribution of the atmospheric aerosol in clear-sky conditions and thin clouds (Wang *et al.*, 2005).

The retrieval theory or the theory of inverse problems from lidar-radar measurements is an active subject of research in atmospheric remote sensing. Analyses of these measurements are based on the theory of propagation of electromagnetic radiation including the backscattering and attenuation processes (Stephens, 1994). Over the years, a number of techniques for determining optical properties from lidar and radar measurements have been developed. They include interactive, nonlinear and statistical solutions. The accuracy of these methods is limited by the assumptions made in forward modelling.

The LITE (Lidar In-space Technology Experiment) mission took place between September 9 and September 20, 1994 (http://www-lite.larc.nasa.gov). It was the first lidar

remote sensing system from space. The LITE lidar provided measurements at three wavelengths: 1064, 353 and 532 *nm*. LITE demonstrated that space-borne backscatter lidar system could provide key information on the vertical structure of aerosol and cloud layers at high resolution on a global scale (Platt and Winker, 1994; Winker *et al.*, 1996). This mission also showed that a space-borne lidar is able to detect a wide range of sizes from air molecules to aerosol and cloud particles. The cloud top can be accurately determined from the lidar signal. It is worth noting that the lidar signal can be completely extinguished in the case of the thick clouds, and deeper detection becomes impossible. Also, the lidar signal can be attenuated extensively by ice clouds and often extinguished by liquid water clouds.

LITE mission demonstrated the potential of application of space-borne lidar in atmospheric remote sensing. The analysis techniques based on LITE data provided the profile retrieval methods for future space-borne lidar missions. Analysis of single-profile data is a complex process. After locating all reflective layers' boundaries, each of them must be identified as being either cloud or aerosol. The range-resolved profiles of optical properties can be derived only if there is prior information about position and composition of each layer (Vaughan *et al.*, 2004). The uncertaintics about position and composition of laycrs strongly depend on the signal-to-noise ratio (SNR) of the measured signal. Because the SNR of space-borne lidar is often low, noise excursions may have magnitudes similar to those of weak cloud or aerosol layers. In addition, the SNR required for the layer detection decreases with altitude because the molecular component of the returned signal, which acts as a noisy background also decreases (NASA PC-SCI-202, 2005).

Multiple scattering cannot be neglected in any detection by lidar. It is considerably higher for a space-borne lidar than in the case of a ground-based lidar (Winker, 1997). This influence is due to the larger field-of-view (FOV) of space-borne lidar. The multiple-scattering effects increase the magnitude of the received signal due to contribution of once scattered photons, which have returned in the lidar FOV in some of subsequent scattering events. Also, an increase of the detected signal may be produced by photons that have been scattered at shallow angles but have remained in the lidar FOV. On the other hand, in the conventional lidar equation the multiple scattering is not taken into consideration. This leads to errors in the quantities derived from the lidar signal. For instance, Wang *et al.* (2005)

studied the impact of multiple scattering on cirrus observed by ground-based Raman lidar. They showed that the evaluated extinction coefficient from lidar measurements could be underestimated by 200 percent while the backscattering coefficient remains unchanged.

For elastic backscatter lidar, the retrieval of cloud properties involves computation of backscatter and extinction from only one measured quantity. Therefore, the lidar ratio (the ratio between extinction and backscattering coefficients) is required as input parameter and must be assumed (Klett, 1981, 1985; Fernald, 1984). Once assumed, it remains constant within a cloud layer. This assumption may be unrealistic in case of small-scale variability in microphysical properties inside the sample volume. Hence, the assumed homogeneous microphysical composition throughout the cloud layer can lead to retrieval uncertainties (Noel *et al.*, 2007).

The aerosol lidar ratio is also assumed to be constant but different for various types of aerosol. It strongly varies both spatially and temporally and depends on the size distribution, shape and composition of aerosol. As such, aerosol lidar ratio can only roughly be estimated from individual measurements. Many studies (Sasano *et al.*, 1985; Kovalev, 1995; Karyampudi *et al.*, 1999; Gobby *et al.*, 2002) showed that an inaccurate assumption of aerosol lidar ratio lead to errors in the retrieval of the aerosol optical properties. However, this limitation can be overcome by employing the high-spectral-resolution (HSR) technique (Grund and Eloranta, 1991; Alvarez *et al.*, 1993; Piironen and Eloranta, 1994). Unlike standard backscattered lidar, a HSR lidar separates the backscattered radiation into a part due to cloud (aerosol) particles and a part due to molecules. Although the HSR lidar technique has an important advantage in relation to that of the conventional backscattered lidar, the complete retrieval procedure remains very complicated.

CloudSAT is the first space-borne cloud radar, launched in April 28, 2006. It is 15 second ahead of CALIPSO (Cloud-Aerosol Lidar and Infrared Pathfinder Satellite Observations) launched at the same time (Winker *et al.*, 2002). Their orbits at 705 *km* altitude are a part of the A-Train constellation of Earth-observing satellites (http://www-calipso.larc.nasa.gov/about/atrain.php). The operational frequency of CloudSAT radar is 94 *GHz*. CALIPSO lidar is a backscatter polarization-sensitive lidar operating at 532 *nm* and

1064 *nm*. Global monitoring of clouds using cloud radar and lidar combinations has made a significant advance in cloud remote sensing (Stephens *et al*, 2002).

Several research groups are currently working on developing retrieval algorithms for the CALIPSO and CloudSAT measurement synergy. The effectiveness of these algorithms is limited to regions where both the radar and the lidar measurements overlap. Because the radar beam footprint is large compared with lidar, the lidar sub-samples the radar footprint. This scale mismatch can be important in small-scale cloud with high variability. Attenuation of the lidar signal in optically thick or mixed-phase clouds is an additional difficulty for the cloud radar-lidar synergy. Therefore, there is a need for retrieval methods complementary to the radar-lidar algorithm. These methods are expected to make use of radiometric measurements and the Doppler radar measurements.

In 2013, the European Space Agency (ESA) satellite mission EarthCARE (Earth Clouds Aerosol and Radiation Explorer) will carry a collocated 94 *GHz* cloud profiling Doppler radar and a high-spectral-resolution (HSR) depolarization lidar (ESA SP-1257 (1), 2001) operating at 354 *nm*. In addition, the Broad-Band Radiometer and the Multi-Spectral Imager (MSI) will complement the payload. The EarthCARE lidar will be the first active remote sensing system from space with the HSR configuration. This type of lidar configuration will enable an easier interpretation of measured signal. Collocated measurements of Doppler cloud radar and HSR lidar are expected to provide more detailed global profiling of cloud and aerosol properties.

The validation of space-borne by ground-based lidar and radar measurements is a complicated task for several reasons. Ground-based stations along the line of satellite flight are scarce so the direct satellite over-flights over ground-based observations' centres are rarely. Due to the speed of satellite, only several cloud (aerosol) vertical profiles that correspond to the number of shots are appropriate to compare to the measurement area of the ground-based lidar. As a consequence, horizontally inhomogeneous aerosol and cloud conditions can lead to significant differences between space-borne and ground-based measurements. Detailed analyses are usually performed with observations from different measurement campaigns (such as Asian Pacific Regional Characterization Experiment-ACE - 1, -2, -Asia; Cloud Lidar And Radar Experiment-CLARE; Asian Atmospheric Particle

Change Studies-APEX -1, -2, -3; Cirrus Regional Studies of Tropical Anvils and Cirrus Layers-Florida Area Cirrus Experiment-CRYSTAL-FACE; Indian Ocean Experiment-INDOEX), because a number of advanced remote sensing and in-situ instruments allow the evaluation of the assumptions applied in retrieval methods. However, there is a wide range of conditions that could introduce various uncertainties through the validation procedure. For instance, the retrieval errors can be produced if cloud content is not homogenously distributed over the instrument footprint. Therefore, different cloud masses, averaged over the footprint can cause the same signal. This phenomenon is called the beam filling effect and has been studied by Davis *et al.* (2006). Other uncertainties include the mismatch in sample volumes of the remote-sensing instruments, the instrument limitations regarding a particle range-size as well as different experimental errors. Thus, much effort is needed to establish a systematic validation approach.

Until recently, no sufficiently accurate vertically resolved global observations of clouds and aerosol have been available to validate their representation in atmospheric models. The A-Train NASA observing satellites (Aqua, CloudSAT, CALIPSO, PARASOL and Aura) allow coordinated observations of the different sensors (Stephens *et al.*, 2002). On the other side, various assumptions related to the cloud and aerosol microphysical properties are used as an input to the inversion algorithms of satellite-based measurements. In recent years, the science community has become aware of the importance of estimating the uncertainties in retrieved cloud properties (Mace *et al.*, 1998; Turner, 2005). Uncertainties associated with the space-borne radar and lidar retrievals are related to major assumptions regarding the shape and size distribution of the hydrometeors. Application of cloud and aerosol retrieved properties includes comparisons with model simulations as well as model parameterization development. It is well known that numerical uncertainties in atmospheric models limit the accuracy of simulations of the mean climate and its variability. On the other hand, the model predictions are realistic in that they explicitly consider the fundamental physical and cloud (aerosol) microphysical processes. In this context, another way to validate atmospheric model by space-borne radar and lidar measurements is to involve the *forward* approach, where an atmospheric model provides the atmospheric state and the cloud and aerosol microphysical properties used to simulate the remotely sensed observations. The recent launch of CloudSAT and Calipso is now opening this possibility of validation. The new data are currently flowing

in with billions of estimated profiles sampling the global atmosphere. In this context, the use of the forward approach provides a serious constrain for the validation of clouds and aerosol in atmospheric models.

This study employs an approach of using a model simulating measurements of space-borne radar and lidar instruments in order to assess a method for validating aerosol and cloud parameterizations in climate models. In this approach, an atmospheric model provides the atmospheric state and microphysical properties of cloud and aerosol. These are used to simulate quantities that would be measured by space-borne radar and lidar. In the absence of space-based measurements, these quantities are compared against the airborne radar and lidar observations. The objective of this study is to demonstrate a new method of validating aerosol and cloud parameterization in climate model. The natural intention of this study leads to its application in extensive diagnostic verifications for all types and locations against the corresponding real atmosphere.

In Chapter 1, the models used in this study are described. Chapter 2 is reserved for the methodology incorporating the model simulating the remotely sensed observations (the forward model) with the atmospheric model. Simulation set-up, observation site and measurements descriptions are described in Chapter 3. Results are discussed in Chapter 4, ending with concluding remarks in Chapter 5.

CHAPTER I

MODEL DESCRIPTION

In the Introduction, the uncertainties associated with the retrieval of the microphysical properties of aerosol and clouds were presented. Also, the concept of the forward approach used in this study was introduced. In this approach, an atmospheric model provides the atmospheric state and microphysical properties of cloud and aerosol. In turn, these are used to simulate quantities that would be measured by remote sensing instruments.

In this Chapter, the models used in this study are summarized for the purposes of this study. Section 1.1 is reserved for the description of the forward model while the atmospheric model complement is described in Section 1.2.

1.1 The EarthCARE Instrument Simulator

The EarthCARE (Earth Clouds Aerosol and Radiation Explorer) is a joint mission of European Space Agency (ESA), Japanese Aerospace Exploration Agency (JAXA) and Japanese National Institute of Communications Technology (NICT). The EarthCARE is satellite scheduled for launch in 2013. It consists of two nadir-sounding active instruments: the Cloud Profiling Radar (CPR) and the backscatter Atmospheric Lidar (ATLID). In addition, the Multi-Spectral Imager (MSI) and the Broad-Band Radiometer (BBR) will complement the payload. All instruments are planned to be co-aligned nadir-viewing and will observe nearly the same volume of the atmosphere at slightly different times. The scientific requirement of the mission is measuring the vertical profiles of clouds and aerosol to derive instantaneous radiative fluxes with an accuracy of 10 Wm^{-2} (ESA SP-1257 (1), 2001). The primary aim of the EarthCARE mission is to determine the global distribution of vertical profiles of aerosol and cloud characteristics, which is an essential component in numerical modelling of the atmosphere.

Within the preparatory studies for EarthCARE, the EarthCARE Instrument Simulator (IS) (Donovan *et al.*, 2004) has been developed. This model simulates measurements of active and passive instruments onboard the EarthCARE satellite in a "radiatively consistent manner", where the difference between radiative fluxes calculated from the physical properties retrieved from the synergetic EarthCARE-simulated measurements and "real" fluxes is within $\pm 10\ Wm^{-2}$ (Donovan *et al.*, 2004). As an input, the model needs various fields of a virtual atmosphere, e.g. the standard atmosphere with cloud/aerosol layers defined by a set of parameters referring to different radiation properties required for instruments' modules. The conceptual structure of the model is shown in Fig. 1.1.

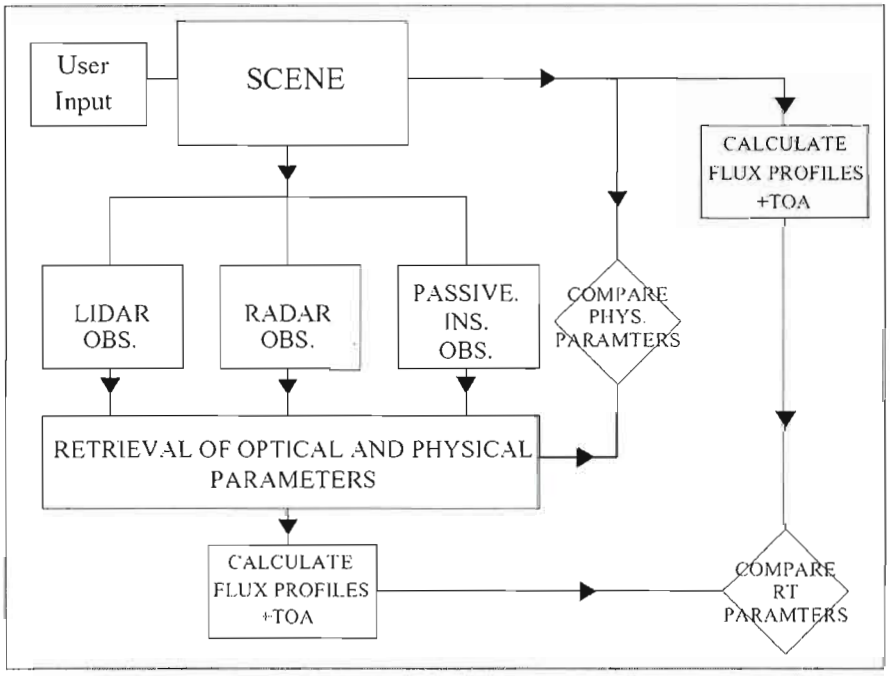

Figure 1.1 Algorithm of the EarthCARE Instrument Simulator

The principal part of the IS model consists of several modules simulating the measurements of active and passive instruments onboard the EarthCARE satellite. Orbit file defines the orbit, the speed and the altitude of satellite. The virtual atmosphere in which measurements are simulated is specified in a so-called Universal File Format (UFF) file.

Here, the term "universal" means that UFF file is accessed by all the elements of the simulator modules. The atmosphere is created by the module "scene creator" and consists of a chosen standard atmosphere and user-defined cloud and aerosol layers. It is worth noting that the parameters referring to different radiation properties required for instruments' modules are not stored in the UFF file but in library files (so-called "scattering libraries") referenced by the UFF file. The instruments' modules as well as the "scene creator " module constitute a group of the forward model programs. The retrieval programs package utilizes the simulated measurements from all instruments in order to restore top-of-atmosphere (TOA) radiative fluxes and to compare these fluxes with those computed by the same radiative transfer code but instead using inputs from the initial atmosphere (Fig. 1.1). Instruments are specified in various modules in the IS. In the following subchapter the properties of the EarthCARE radar and lidar instruments are summarized.

1.1.1 Radar and Lidar Instrument Description

The Cloud Profiling Radar is millimetre-wave radar with Doppler capability designed to provide vertical profiles of cloud structure along the satellite track. The frequency of the CPR is 94.05 *GHz* with a pulse length of 3.3 microseconds providing 500-*m* vertical resolution. A 94 *GHz* cloud profiling radar is able to penetrate ice clouds with negligible attenuation and provide a range-gated profile of cloud characteristics. The effective vertical resolution, defined as the half-power width of the impulse response function, is 385 *m*. A 2.5-*m* antenna and a 400-*km* orbit give a footprint of about 600 *m*. The expected sensitivity of the radar, given in terms of the minimum detectable reflectivity, is –35 *dBZ*. The instrument characteristics are summarized in Table 1.1.

Table 1.1 Characteristics of the EarthCARE Lidar Instrument

INSTRUMENT	EarthCARE Radar
Satellite	Altitude 400 km, orbit speed 7 km/sec
Radar	Short pulse radar, nadir looking
Frequency	94 GHz (≈ 3.2 mm)
Emitted power	300 W
Pulse Repetition Frequency	6800 Hz
Antenna diameter	2.5 m
Sensitivity	≈ -36 dBZ
Horizontal Resolution	0.65 - 1 km
Vertical Resolution	400 m
Doppler capability	yes

The EarthCARE atmospheric lidar is a single-wavelength (353 *nm*) depolarization lidar with a high-spectral-resolution receiver separating molecular backscatter ("Rayleigh") from the aerosol and cloud backscatter ("Mie") returns (ESA SP-1279 (1), 2004). The laser beam is right-hand circularly polarized and the receiver subsystem is designed to detect changes in the polarization state of the collected backscattered return. The polarization beam splinter separates the backscattered intensities into two orthogonal polarization components. One component is parallel while the other is perpendicular to the polarization plane of the transmitted laser beam. Mie and Rayleigh contributions are separated by HSR Fabry-Pérot etalons, which are also useful for the suppression of background radiation. Three receiver channels are to be provided: Mie co- and cross-polar, as well as Rayleigh co-polar. ATLID is a nadir looking lidar with an offset of 2° in the along-track forward direction, with a footprint of approximately 20 *m*. The lidar is designed to provide vertical profiles of the atmosphere from the ground up to 20-*km* altitude with 100-*m* vertical resolution. The main characteristics

of the instrument are shown on Table 1.2. Detailed characteristics of the EarthCARE lidar and radar instruments used in this study are given in ESA SP-1279 (1) (2004).

Table 1.2 Characteristics of the EarthCARE Lidar Instrument

INSTRUMENT	EarthCARE Lidar
Laser	Tripled Nd:Yag, 35 mJ, HSR, right circularly polarized
Wavelength	353 nm
Footprint	20 m (12 or 5 m)
Pulse Repetition Frequency	70 Hz
Receiver Telescope	0.6 m diameter
Polarization	Mie parallel, Raleigh parallel, total perpendicular
Vertical Resolution	100 -250 m
Horizontal Resolution	100 m

1.1.2 Radar and lidar remote sensing: Theoretical background

Radar and lidar remote sensing are techniques in which a radiation signal is used to provide range-resolved remote sounding of the atmosphere. Both instruments make measurements by emitting a pulse of electromagnetic energy into the atmosphere. As the pulse propagates, the energy is continuously absorbed and scattered by the molecules of the atmosphere (lidar) and by aerosol (lidar) and/or cloud (lidar and radar) particles. Some fraction of the emitted energy is reflected back toward the instrument receiver subsystem. The collected backscattered energy is then filtered and amplified using both optical and electronic signal processing techniques and finally recorded in digital data storage system. By measuring the time between transmission and reception, the distance of the scattering object (range) is estimated. The principal difference between radar and lidar is the wavelength of the

radiation used. Radar transmits a pulse of microwave energy to the atmosphere, whereas lidar transmits energy on shorter wavelengths- ultraviolet (UV), visible or infrared radiation generated by lasers. The different wavelengths used by instruments differ by about three orders of the magnitude and therefore lead to the very different forms of actual measurements.

Quantitative analyses of lidar and radar detection techniques result from the mathematical expressions that relate received power to the transmitted power. Both lidar and radar equations include the physical processes involved by the propagation of the radiation beam through atmosphere and its interaction with atmospheric constituents. The expression for the radar cloud return is considerably simpler than for the lidar as only single scattering is important at the cloud radar frequencies. Most cloud radars operate at 35 *GHz* and 94 *GHz*. The radar signal is due to Rayleigh scattering and the lidar signal is due to the Mie scattering, which makes the two instruments differently sensitive to the size of particles and consequently to the vertical distribution of ice (water) inside clouds. Both radar and lidar measurements are related to the particle size distribution; radar reflectivity factor is approximately proportional to the sixth power of particle size while the lidar return is related to particle size to the power of two. In the following sections radar and lidar modules are described further.

1.1.3 Radar module

The cloud water droplets are very small compared to the wavelength of the EarthCARE CPR (3.2 *mm*). Hence, the radar echo intensity increases with the inverse-fourth power of the wavelength and is due to Rayleigh scattering. Ice cloud particles although much bigger than the water droplets could be still small compared to the radar wavelength, and thus could be also treated as Rayleigh scatters. Assuming that the radar echoing mechanism is due to the Rayleigh scattering, the received signal from the EarthCARE CPR is determined by the radar equation:

$$P_r = \frac{C_{rad}|K|^2}{R^2} Z_M \,, \tag{1}$$

where P_r is the mean received power; C_{rad} is the radar constant that includes system characteristics as the transmitted power, the radar resolution range and the antenna pattern; R is the distance of the radar volume under consideration; K is the factor that incorporates the refractive index of the scattering cloud particles and Z_M is the "apparent" or "measured" radar reflectivity factor. The term "apparent" refers to the reflectivity measured by a space-borne radar system, and thus to the values not corrected for the atmospheric attenuation and strongly dependent on the characteristics of a particular remote sensing measurement system.

Using scattering theory, cloud parameters related to the radar measurements can be derived from the particle size distribution. The definition of the effective radar reflectivity factor in the EarthCARE radar module has been slightly modified by taking into account different behaviours of the radar backscattering signal at wavelengths of 94 *GHz* and 3 *GHz* (Donovan *et al.*, 2004). This distinction is governed by the fact that the refractive index of water, through the dialectic factor, is not constant with respect to frequency and temperature. Indeed, the refractive index of water is sensitive to temperature at 94 *GHz* while largely insensitive at 3 *GHz*. The equivalent radar reflectivity Z_e is defined as the effective reflectivity that would be observed at 3 *GHz*:

$$Z_e \equiv \frac{1}{|K_{w,3GHz}|^2} \frac{\lambda^4}{\pi^5} \int N(D)\sigma_b(D)\, dD \,, \tag{2}$$

where N is the number of cloud particles per cubic meter and per interval of diameter D, λ is the radar frequency, $|K_{W,3Ghz}|^2$ is the dielectric factor for water at 3 *GHz*, and $\sigma_b(D)$ is the backscattering cross-section for droplets of diameter D. The backscattering cross-section can be derived from Mie theory for $D<<\lambda$, and is given by:

$$\sigma_b(D) = \frac{\pi^5}{\lambda^4} D^6 |K|^2 \,. \tag{3}$$

The EarthCARE CPR equivalent reflectivity for water cloud particles as well as for ice particles is given, respectively, by:

$$Z_e = \frac{|K_{W,94GHz}(T)|^2}{|K_{W,3GHz}|^2} \int N(D) D^6 dD, \tag{4a}$$

$$Z_e = \frac{|K_{W,94GHz}(T)|^2}{|K_{W,3GHz}|^2} \frac{\rho_w}{\rho_i} \int N(D_{eq}) D_{eq}^6 dD_{eq}, \tag{4b}$$

where D_{eq} is the equivalent melted diameter of the particle (i.e., the diameter of the spheres of the same volume), while ρ_w and ρ_i are densities of water and ice respectively. It is assumed in Equation (4b) that the diameter of ice particles is small enough to obey Rayleigh approximation.

The Equations (4) describe the approach used in EarthCARE radar module to compute reflectivity from the specified parameters characterizing the considered cloud structure. Computed values are referred to as the "true values" of the radar reflectivity factor. All quantities on the right-hand side of these equations are supposed to be known, i.e. they are given or computed from the input.

The EarthCARE radar simulator is composed of four modules allowing retrieving the reflectivity profiles "measured" by the radar from the "true" reflectivity factor. These modules are: Attenuation Module, Beam Filling Effect Module, Noise Module and Convolution Module. The Attenuation Module accounts for the signal attenuation through the atmosphere and cloud layers in the satellite geometry. The attenuated radar reflectivity factor Z_a (in units of $dB\ km^{-1}$) is expressed as:

$$Z_a(h) = Z_e(h) \exp\left(-2 \int_h^{100km} K_t(z) dz\right), \tag{5}$$

where Z_e is the "true" radar reflectivity factor on the height h, and K_t is the total attenuation coefficient due to gases and hydrometeors from a height h to the top of atmosphere (modelled as 100 km). The total attenuation coefficient K_t is modelled as:

$$K_t = K_v + K_h, \tag{6}$$

where K_v is the attenuation by water vapour, and K_h is the attenuation by hydrometeors. The attenuation due to the hydrometeors is a known parameter determined from the cloud system

under consideration. The attenuation due to water vapour is modelled according to Ulaby formulation (Ulaby *et al.*, 1981) for frequencies between 1 *GHz* and 100 *GHz* and is given by:

$$K_v[dB/km] = 2f^2\rho_v\left(\frac{300}{T}\right)^{3/2}\left(\frac{\frac{300}{T}\exp(-644/T)}{\left(494.4-f^2\right)^2-4f^2\varsigma^2}+1.2\times10^{-6}\right), \tag{7}$$

where f is the frequency in *GHz*, T is the absolute temperature, ρ_v is the density of water vapour in gm^{-3} and ς is a function of pressure, temperature and density of water vapour given by:

$$\varsigma = 2.85\left(\frac{p}{1013}\right)\left(\frac{300}{T}\right)^{0.626}\left(1+0.18\rho_v\frac{T}{p}\right). \tag{8}$$

At frequencies of 3 *GHz* and 94 *GHz* the attenuation by gases other than water vapour is mainly due to oxygen (O_2). The absorption coefficient for oxygen is approximately 0.03 $dB\ km^{-1}$ at 94 *GHz* and it is neglected (Donovan *et al.*, 2004).

Characteristics of a radar measurement system itself also contribute to the difference between the true and the measured radar reflectivity profile. The factors regarded as important to estimate these differences are related to the modelling of the horizontally-averaged reflectivity as well as of the vertical sampling frequency, the modelling of the speckle and thermal noise (receiver-related noise), and the computing of the effect of range weighting due to the finite width of the transmitted pulse. The Beam Filling Effect Module takes into account the spatial integration while the Noise Module simulates the effects of the speckle noise related to the statistics of the signal itself and thermal or receiver related noise. Finally, the Convolution Module generates the measured cloud profiles by simulating radar transfer functions. The noise characteristics are appropriately scaled in order to account for the over-sampling of the radar signal. Detailed descriptions of the used algorithms are given by (Donovan *et al.*, 2004).

1.1.4 Lidar module

The single-scattering signal received by a lidar system from the atmospheric backscattering at a distance z is given by the lidar equation:

$$P_r(R,\lambda) = C_{lid}\frac{\beta_\pi(R,\lambda)}{R^2}\exp\left[-2\int_0^R \beta_e(z,\lambda)dz\right], \tag{9}$$

where P_r is the total power detected by the lidar system from a target at distance R from the lidar, λ is the laser wavelength, C_{lid} is a constant containing all system parameters, β_π is the backscattering coefficient and β_e is the extinction coefficient. Equation (9) is valid only when single-scattering events are dominant.

In the conventional solution of backscattered lidar signals, it is well known that multiple scattering influences measurements in clouds and that these effects lead to errors in the quantities derived from the lidar signal. Multiple scattering on the lidar signal depends on the characteristics of the lidar system as well as of the atmosphere under consideration. In general, multiple scattering cannot be neglected if the mean free path of photons is small compared to the lidar sampling volume, or if the angular width of the scatterer's forward scattering lobe is not much larger than the angular width of the receiver's field of view (Donovan *et al.*, 2004). The critical parameters determining the contributions of multiple scattering are: the ratio of laser divergence angle to the telescope field-of-view, the range from the lidar, the optical depth from the lidar to the target plane, and the width of the forward scattering lobe.

The EarthCARE lidar signal is computed using semi-analytical Monte-Carlo method – an hybrid approach that takes into account of multiple scattering effects and also increases the computational efficiency versus a standard Monte-Carlo method (Donovan *et al.*, 2004) The semi-analytical Monte-Carlo method is based on computer modelling of photon trajectories by incorporating statistical treatment of free-path lengths and scattering angles. First, the amount of un-scattered energy from the lidar is analytically calculated at each altitude. Secondly, a number of appropriately weighted photons trajectories are fallowed in order to compute the higher scattering orders. The amount of the signal received by the lidar telescope is added for each scattering event. The computational efficiency is implemented by forcing

the photons scattering to occur within a specified distance from the receiver axis (Platt, 1981). Also, the number of backscattering events is increased by the technique of using symmetric effective phase function such that more photons travel toward the receiver but with a suitably reduced weight as described by Platt (1981).

The lidar receiver consists of a number of elements operating at the spectral and polarization state of the lidar return. The polarization elements are assumed to act perfectly while the broadband spectral filters are modelled as having a rectangular pass-band and are characterized by a single in-band transmission-reflection pair and an out-of-band reflection-transmission pair. The most important optical element is the Fabry-Pérot etalon used to separate Mie signal from the Rayleigh signal; this is modelled according to the approach of Saleh and Teich (1991).

The number of photons arriving at a each detector channel, N_{dec}, for a given time interval Δt, is given by:

$$N_{dec} = \frac{\lambda}{\kappa c}\left(P_r + P_{back}\right)\Delta t\,, \tag{10}$$

where λ is the wavelength for the detector channel, κ is the Planck's constant, c is the speed of light, P_r is the mean power received from the lidar and P_{back} is the mean background power. The background power refers to the power registered by the lidar receiver that is due to the detection of photons from sources other than the laser. It is assumed that the main source of backscattered light is the atmosphere as well as the scattered sunlight from the Earth surface and, as such, depends on the solar angle, the surface type, the cloud cover and the receiver instrument characteristics. All other sources (i.e., moon light, stars, sun light scattered by atmospheric particles and air) are neglected.

Noise refers to random variations in the measured signals unrelated to the received light intensity, causing a corresponding uncertainty in the values measured by the lidar detector subsystem. The noise contribution is expressed in the terms of the equivalent fluctuations of the number of photons arriving at the detector and assuming standard Gaussian statistics. Three sources of noise are considered: detector dark-current, background (statistical fluctuation of the sunlit background) and instrument-related noise. It is worth

mentioning that the latter is dependent on the magnitude of the detected signal and receiver's optics.

1.2 NARCM configuration

Northern Aerosol Regional Climate Model (NARCM) (Spacek *et al.*, 1999) is a limited-area non-hydrostatic dynamical model based on the Canadian Regional Climate Model (CRCM) and Canadian Aerosol Module (CAM). The NARCM physical parameterizations are imported from the Canadian General Circulation Climate Model (GCCM) (McFarlane *et al.*, 1992; Zhang and McFarlane, 1995) while its dynamical kernel is identical to the CRCM (Laprise *et al.*, 1997; Caya and Laprise, 1999). It is based on the fully elastic, non-hydrostatic Euler equations solved with semi-Lagrangian and semi-implicit transport scheme for dynamics and passive tracers (Robert *et al.*, 1985). The horizontal domain consists of a polar-stereographic projection on Arakawa C staggered grid arrangement with terrain-following Gal-Chan vertical coordinate. The physical parameterizations package takes into account radiation, gravity wave drag, turbulent diffusion, surface processes and cloud microphysics. Vertical fluxes of momentum, heat and moisture due to turbulent transfer processes are represented using a mixing-length formulation in the free atmosphere and are calculated from Monin-Obukhov similarity theory at the surface. A cloud microphysical scheme for stratiform clouds (Lohmann and Roeckner, 1996) is included into the physical package. The stratiform cloud scheme solves separate prognostic equations for cloud water and cloud ice. Microphysical processes included in this scheme are: condensational growth of cloud droplets, depositional growth of ice crystals, homogeneous, heterogeneous and contact freezing of cloud droplets, auto-conversion of cloud droplets, aggregation of ice crystals, accretion of cloud ice and cloud droplets by snow and by rain, evaporation of cloud water and rain, sublimation of cloud ice and snow and melting of cloud ice and snow.

NARCM aerosol processes are based on Canadian Aerosol Module (Gong *et al.*, 2003), which accounts for five aerosol species (tracers): sea-salt, sulphate, black carbon,

organic carbon and soil dust provided by the chemical transport models (Penner *et al.*, 1992; Chin *et al.*, 1996; Tegen *et al.*, 1997; Gong *et al.*, 1997; Graf *et al.*, 1997). The particle size distribution is modelled by representing the size spectrum of each aerosol component as a series of twelve size bins partitioned at multiples-of-two radii between 0.005 and 20.48 μm. Each aerosol size section is represented by one mass-conserving prognostic equation including processes such as surface emission rate of both natural and anthropogenic aerosol, production of secondary aerosol (airborne aerosol mass produced by chemical transformation of their precursors), nucleation, condensation and coagulation, aerosol transport, dry deposition, hygroscopic growth and interaction with clouds as well as wet removal. The aerosol transport, including the processes of 3-D advection as well as sub-grid turbulent diffusion and convection, is carried out by the GCM. It is assumed that aerosol components are internally mixed within each size bin except for the freshly emitted insoluble components (black carbon and soil dust), which are treated as externally mixed for a fixed amount of time (one integration time step). The number densities of externally-mixed aerosol components are calculated for every time step and then used to estimate the aerosol activation and radiative forcing.

1.2.1 Lohmann microphysics

The NARCM cloud microphysics is based on a bulk scheme developed by Lohmann and Roeckner (1996). Cloud water, cloud ice and total cloud water (water and ice) are treated as separate prognostic variables. The precipitation generating mechanism considers both maritime and continental warm clouds by taking into account the number distribution of cloud droplets in addition to the liquid water content. Only sulphate aerosol components are treated as the source of cloud condensation nuclei (CCN). The shape of all hydrometeors is assumed to be spherical. Some of the aspects of the Lohmann scheme are described below.

It is assumed that there are always sufficient condensation nuclei so the condensational growth of cloud droplets occurs at temperatures above –35° C as soon as the value of the critical diameter and relative humidity threshold (100 %) are exceeded. The depositional

growth of water vapour on ice crystal always occurs at the temperatures below –35° C, and can occur above –35° C only if cloud ice is already present. The conversion of cloud droplets into ice crystals is regulated by homogeneous and instantaneous freezing of total amount of cloud water at the temperatures above –35° C and by stochastic, heterogeneous and contact freezing below –35° C. The rate of stochastic and heterogeneous freezing is a function of the temperature, the amount of cloud water and the present amount of CCN. The contact-freezing rate is parameterized as the freezing of an amount of cloud droplets resulting from random collision of aerosol particles with the super cooled cloud droplets and as such depending of the amount of CCN.

In the microphysics scheme used by version 3 of NARCM, it is assumed that only sulphate aerosol can act as cloud condensation nuclei. As the used parameterization of heterogeneous freezing depends on cloud droplet size and number, the forming ice can be affected by changes in sulphate load. However, the indirect effect based on this assumption can be hardly estimated, as there is no prognostic equation for the number concentration of ice crystals. Furthermore, it is not assumed that aerosol can act as ice nuclei (IN). The ice nucleation processes have been introduced in the later version of NARCM (Girard and Blanchet, 2001) and organic carbon, sea-salt and black carbon have been added as candidates of CCN (Hu et al, 2005).

CHAPTER II

METHODOLOGY

Generally speaking, NARCM simulations can be employed to generate suitable datasets for instrument modules. As it was mentioned before, UFF file represents an input for the Simulator modules and contains data to build a virtual atmosphere over which simulated measurements can be made. These data are required to be altitude-dependent and at fixed vertical and horizontal resolution.

Horizontal and vertical resolutions of radar and lidar simulated measurements correspond to the fundamental sampling resolution of the instruments i.e., to the resolution at which raw profile data would be stored in digital data storage systems. The fundamental sampling resolution is determined by the receiver electrical bandwidth and the pulse repetition rate. Generally, the horizontal resolution represents the horizontal distance between two successive transmitted pulses while the vertical resolution varies with altitude and depends on the spatial scales of the predominant features expected being measured. Usually, the instrument resolution is highest in the mid troposphere (5-7 *km*) where the spatial variability of clouds and aerosol is greatest and becomes lower higher in the atmosphere. However, resolution of atmospheric data contained in UFF file must be greater or equal to the highest resolution of the considered instruments. This implies some difficulties in employing regional atmospheric models to generate an appropriate input dataset in order to simulate space-borne radar and lidar measurements. The instrument horizontal resolution is much higher than the resolution utilized in regional simulations of an atmospheric model. This difference is typically about three or two orders of magnitude. For example, the horizontal resolution utilized in regional simulations of atmospheric model is usually 45 *km* while the along-track resolution of the proposed EarthCARE lidar and radar measurements is about 20 *m* and 1 *km*, respectively. Therefore, it is feasible to associate a single column of the regional climate model with *an individual simulated vertical profile* representing the average of measured profiles within the model grid column.

It is worth noting that different aerosol and hydrometeor classes specified in UFF file must be compatible with those already present in the Simulator "scattering libraries". The IS aerosol and cloud categories referred to as "scattering types" are presented in Table 2.1. As it can be seen from Table 2.1, their size spectrum is divided into a specified number of particle sizes. For every single-particle bin radius, data stored in scattering libraries contain the corresponding volume, area, extinction and absorption cross-section, and scattering phase function at high angular resolution, all for specified types of aerosol and clouds. The data cover wavelengths from 200 *nm* to 4000 μm at approximately 166 discrete wavelengths and include radar frequency of 94 *GHz*.

The most critical part of the UFF file is the size-segregated number concentration for each hydrometeor category and aerosol component. Their bin number and bin size as already specified in library files must correspond to bin number concentrations present in UFF file. Aerosol size distributions are computed by NARCM, but cloud-resolving scheme gives only total mass content for two hydrometeor categories. Concerning aerosol scattering data included in the Simulator model, an inspection of Table 2.1 shows that they were made under the assumption that the aerosol optical properties are not sensitive to the ambient relative humidity, there is no computed radiative quantities for organic carbon, and the assumed aerosol size spectrum in IS libraries is narrower than in the case of NARCM aerosol.

As the NARCM fields cannot be directly employed to create the required input for Instrument Simulator, an algorithm creating UFF input file from the NARCM produced quantities is developed. The NARCM fields used as input for the module are: temperature, relative humidity, specific humidity, surface pressure, wind, water and ice mass content as well as aerosol mass concentration. After altitude-to-pressure (*z-p*) conversion, these fields are linearly interpolated to the IS vertical resolution below 15 *km*. NARCM 45-*km* grid-resolved *individual* vertical fields are rearranged such that the distance between any two grid-points corresponds to the length of the lidar footprint. The top of the IS atmosphere, fixed at 100 *km* is set to altitudes between 10 and 15 *km*, depending on the height of the troposphere (assuming empty space lies above of these altitudes). The code of instrument modules is adjusted for this correction.

In addition, modifications are needed inside the IS lidar code regarding the vertical (and horizontal) variability of different radiative properties. Namely, the lidar and radar codes have been built assuming that a rectangular hydrometeor layer was completely specified with its position (in the Cartesian coordinate system), type (Table 2.1), and the effective radius and water content (or aerosol mass concentration) specified at least at its base and top. Bin-number distributions for all hydrometeor types are supposed to be computed in function of effective radius and water content by using the modified-gamma distribution (Walko *et al.*, 1995). These assumptions imply that the radiative properties (e.g., elements of the scattering matrix and scattering coefficients) of the hydrometeor layer would change vertically but remain homogeneous in the horizontal direction.

Furthermore, although the cross-sections and scattering phase function for cloud water were computed in a function of wavelength and the temperature dependent complex refractive index, the vertical variability of temperature in computing the radiative properties is not accounted in the IS instruments' modules. Also, the lidar code does not account for the aerosol radiative properties in a function of relative humidity but for dry aerosol.

The following assumptions from the original EarthCARE IS (Donovan *et al.*, 2004) are modified. The specification of rectangular layers' boundaries is excluded by allowing every grid-point to have zero or non-zero values in water content (aerosol mass concentration). As the aerosol number densities are prognostically computed by NARCM, the hydrometeor effective radius is involved only in the grid-points characterized by an amount in (liquid and/or ice) water content, and thus allowing the computation of corresponding bin-number distributions according to the modified-gamma distribution. In addition, the EC instruments' codes are revised in order to allow the computing the elements of the scattering matrix and scattering coefficients in a function of temperature and relative humidity in addition to wavelength and the particle size distribution.

Table 2.3 "Scattering libraries" of the Instrument Simulator

NAME	r_{min}	r_{max}	N° of sizes
Cloud Water	1.0	50.0	50
Drizzle	10.0	500.0	10
Sulphates (25 %)	0.01	10.0	30
Sulphates (25 %)	0.01	10.0	30
Sulphates (25 %)	0.01	10.0	30
Soot	0.01	10.0	30
Sea Salt	0.01	10.0	30
Dust	0.01	10.0	30
Columns (perfect)	1.75	650.0	8
Columns (rough)	1.75	650.0	8
Plates (perfect)	15.0	650.0	6
Plates (rough)	15.0	650.0	6
Ice	0.5	50.0	50
Snow	25.0	2500.0	50

With these improvements to the original code, the simulation allows the treatment of complex inhomogeneous and moist aerosol from 3D field of simulated dry aerosol. This is more realistic for comparison against observed measurements.

The computation of ice and liquid number concentrations is described in Section 2.1, while the approach related to the treatment of aerosol is presented in Section 2.2.

2.1 NARCM cloud microphysics and EarthCARE Simulator input parameters

The NARCM cloud microphysics is based on the Lohmann bulk scheme (Lohmann and Roeckner, 1996) that includes prognostic treatment of the cloud water and cloud ice. The particle size distribution represents a part of the input to the radar and lidar modules in the EC Simulator. This information is supplied by assuming that the number of cloud particles per unit volume of air is distributed according to the modified-gamma distribution described by Walko *et al.* (1995) and used by Donovan *et al.* (2004):

$$n(\xi) = \frac{N_0}{\Gamma(\gamma)\xi_m}\left(\frac{\xi}{\xi_m}\right)^{\gamma-1} \exp\left(-\xi/\xi_m\right), \tag{11}$$

where $n(\xi)$ is the number density concentration with ξ representing the droplet volume radius for liquid hydrometeors and a particle diameter for solid hydrometeor category, ξ_m is the distribution characteristic size of a category, N_0 is the total number concentration of particles per unit volume of air (in cm^{-3}) and γ is a constant that defines the shape of the distribution such that large values of γ correspond to a broad distribution.

The distribution characteristic size ξ_m is related to ξ according to the following:

$$\gamma\xi_m = \frac{\int_0^\infty \xi\, n(\xi)\, d\xi}{\int_0^\infty n(\xi)\, d\xi} = \bar{\xi}. \tag{12}$$

Here, $\bar{\xi}$ describes the size of the particle having a mean mass and it is equal to the water content of a given hydrometeor category divided by its number concentration. Note that $\bar{\xi}$ defined on this way involves the hydrometeor bulk density into consideration. For a single mode distribution, the equivalent radius r_e is related to the characteristic size of a hydrometeor category as follows (Hu and Stamnes, 1993):

$$r_e = \xi_m(\gamma+2). \tag{13}$$

The shape parameter $\gamma = 2$ is defined as a constant value for hydrometeor classes. Therefore, knowing the effective radius of the cloud particles and the cloud water content at any grid-

point, it is straightforward to compute the fraction of hydrometeors of a given category per unit air volume $n(\xi)d\xi$ occurring at a given value of ξ.

For liquid clouds, the mean volume cloud droplet radius r_v is defined in NARCM as

$$r_v = \sqrt[3]{\frac{3q_{cl}}{4\pi\rho_w N_l}}, \tag{14}$$

where q_{cl} is the cloud liquid water content, ρ_w is the density of water (1000 $kg\ m^{-3}$) and N_l represents the cloud droplet number concentration. The cloud droplet number concentration N_l^{mar} and N_l^{cont} for maritime and continental clouds, respectively, are empirically related to the sulphate aerosol mass m_{sulf} (Boucher and Lohmann, 1995) as follows:

$$N_l^{mar}(m^{-3}) = 10^6 10^{2.06+0.48\log(m_{sulf}(\mu g\, m^{-3}))}, \tag{15a}$$

$$N_l^{cont}(m^{-3}) = 10^6 10^{2.24+0.257\log(m_{sulf}(\mu g\, m^{-3}))}. \tag{15b}$$

The effective radius r_e and the mean volume radius are linearly related (Johnson, 1993; used by Lohmann and Roeckner, 1996) as

$$r_e = c_o r_v, \tag{16}$$

with c_o=1.143 for continental clouds and c_o=1.077 for maritime clouds. The effective radius of ice crystals is parameterized according to an empirical relationship between the effective radius of an ice crystal distribution and the observations of the ice water content based on aircraft observations of frontal clouds around the British Isles (Moss and Johnson, 1994; used by Lohmann and Roeckner, 1996):

$$r_e(m) = c_1 10^{-6}\left(10^3 q_{cl}\right)^{c_2}, \tag{17}$$

where c_1=83.8 and c_2=0.216.

In this study, two experiments are performed. While the effective radius for cloud liquid droplets is computed by Equations (14) to (16), in the first experiment the ice crystal effective radius is computed using Equation (17), and in the second experiment the effective

radius is parameterized as a function of the temperature based on the observations for mid-latitude cirrus described by Ou and Liou (1995) and used by Lohmann (2002) as:

$$r_e = 0.5\times10^{-6}\left[326.3 + 12.4(T - T_0) + 0.2(T - T_0)^2 + 0.001(T - T_0)^3\right], \quad (18)$$

where T_0=273.16 K and r_e is in meters.

2.2 Aerosol optical properties

In the present study aerosol optical properties are computed utilizing the Aerosol Optical Parameters Module (AOPM) of the Canadian Aerosol Module – Third Generation Canadian Climate Centre General Circulation Model III (CAM-CCC GCM III), generously provided to us by Tarek Ayash and Sunling Gong (Ayash *et al.*, 2008).

This scheme, which is applied for diagnostic purposes and to compute an input for radiation code, provides the following quantities: a) column integrated optical depth, single-scattering albedo and asymmetry factor at four specific wavelengths (0.44, 0.50 0.55 and 0.67 μm); and b) vertical-resolved optical depth, single-scattering albedo and asymmetry factor for solar bands and absorption optical depth for terrestrial bands. These quantities are computed from tabulated optical parameters (look–up tables) calculated by a Mie algorithm.

The look-up tables contain band-averaged and wavelength-specific asymmetry factor as well as absorption and scattering cross sections for CAM's aerosol types and size bins, all for thirteen relative humidity classes. As these tables do not provide the optical properties at lidar wavelengths for EarthCARE and Calipso, new look-up tables are generated and the original code had to be modified in order to provide lidar ratio and (attenuated and non-attenuated) backscatter coefficient.

Real and complex indexes of refraction for five aerosol components are obtained from the OPAC (Optical Properties of Aerosol and Clouds) database (Hess *et al., 1998*) for eight values of relative humidity: 0%, 50%, 70%, 80%, 90%, 95%, 98% and 99%, all at wavelengths 350, 500, 550, 1000 and 10025 *nm*. For each of the specified OPAC humidity

classes, aerosol refractive index values (real and imaginary part) for wavelengths 353, 523 and 1064 *nm* are determined by performing linear interpolation. In order to refine refractive index values in the entire range of relative humidity for our wavelengths of interest, humidity classes of 10, 20, 30, 40 and 60 % are added to the above list. Real and imaginary parts of refractive index for these humidity classes are inserted by their estimation from surrounding known values as a function of wavelength, relative humidity, and aerosol materials.

Although water uptake is accounted for in various microphysical processes, NARCM aerosol do not include explicitly condensed water as an aerosol component. In complement, it must be calculated. For this purpose, it is supposed that for those aerosols up taking water, the mode radius remains unchanged while their optical properties change according to composition. This change is taken into account through the values of complex refractive index due to increasing water content of humid aerosol. The particle refractive index changes toward the refractive index of pure water as water amount increases. On the other hand, optical parameters of hydrophobic soil dust and black carbon particles do not depend on relative humidity and their refractive index remain identical to those of dry matter.

Similar to the approach used in AOPM, the aerosol is assumed to be an external mixture of each species for every single size-bin component on the aerosol spectra. This assumption permits to describe the wide range of possible aerosol compositions resulting from independent particles from different sources and processes in the atmosphere. The extinction, scattering and backscatter coefficients are calculated for each species and size-bin as well as for the sum of size bin components.

These optical properties are computed by applying Mie scattering theory for spherical particles. A standard Mie code (extracted from EarthCARE IS package) is used to compute scattering and extinction efficiencies as well as two scattering functions for twelve NARCM's size bin radii and five species, four wavelengths (353, 500, 523 and 1064 *nm*) and thirteen classes of relative humidity for soluble components. In addition, four elements of Mie scattering matrix P_{11}, P_{12}, P_{33} and P_{34} are evaluated following Liou (2002):

$$\frac{P_{11}(\theta)}{4\pi} = \frac{1}{2k^2\sigma_s}\left[|S_1(\theta)|^2 + |S_2(\theta)|^2\right], \tag{19a}$$

$$\frac{P_{12}(\theta)}{4\pi} = \frac{1}{2k^2\sigma_s}\left[|S_2(\theta)|^2 - |S_1(\theta)|^2\right], \tag{19b}$$

$$\frac{P_{33}(\theta)}{4\pi} = \frac{1}{2k^2\sigma_s}\left[S_2(\theta)S_1^*(\theta) + S_1(\theta)S_2^*(\theta)\right], \tag{19c}$$

$$\frac{P_{34}(\theta)}{4\pi} = \frac{1}{2k^2\sigma_s}\left[S_2(\theta)S_1^*(\theta) - S_1(\theta)S_2^*(\theta)\right], \tag{19d}$$

where $S_1(\theta)$ and $S_2(\theta)$ are two scattering functions depending on the scattering angle θ, k is the dimensionless size parameter defined as $k=2\pi\lambda^{-1}$. Scattering cross section, σ_s, is determined from corresponding efficiency as $\sigma_s=\pi a^2$, where a represents aerosol bin radius. The asterisk denotes the complex conjugate.

Mie computations are performed within each size-bin for five aerosol components, at four wavelengths and for the values of real and imaginary part of reflective index corresponding to thirteen different humidity classes. Scattering and extinction cross sections are then determined from the corresponding scattering efficiencies. The phase function is evaluated from Equation (19a) and satisfying the normalization condition:

$$\int_0^{2\pi}\int_0^{\pi}\frac{P_{11}(\theta)}{4\pi}\sin\theta d\theta d\phi = 1. \tag{20}$$

Here, P_{11} element represents the phase function, while the solid angle differential expressed in polar coordinates, with θ the polar angle and Φ the azimuthal angle, is given by $\sin\theta\, d\theta\, d\Phi$.

Backscattering cross section σ_π is obtained from the fractional amount of the incident radiation scattered into the reverse direction of the incident beam ($\theta=\pi$) per unit of solid angle. It is computed via following expression:

$$\sigma_\pi = \sigma_s P(\pi), \tag{21}$$

where $P(\pi)$ is the phase function at $\theta=\pi$.

Tabulated cross sections are normalized to a number density of 1 particle per μm^3, and actual coefficients can then be easily obtained by multiplication with total number density

computed prognostically by NARCM. Thus, our optical code provides vertical profiles of the extinction, scattering and backscatter coefficients, attenuated backscatter, single-scattering albedo, lidar ratio (extinction to backscattering ratio) and column-integrated optical depth, all for every aerosol specie as well as for an external mixing of every size bin of each aerosol component.

Firstly, cross sections are re-computed as a function of the actual relative humidity and then scattering, extinction and backscatter coefficients (β_s, β_e, β_π, respectively) for each aerosol component are determined by:

$$\beta_s(\lambda,tr,z_k)=\sum_i \sigma_s(tr,\lambda,i,z_k)\frac{\zeta(tr,i,z_k)}{V(i)\rho(tr)}, \tag{22a}$$

$$\beta_e(\lambda,tr,z_k)=\sum_i \sigma_e(tr,\lambda,i,z_k)\frac{\zeta(tr,i,z_k)}{V(i)\rho(tr)}, \tag{22b}$$

$$\beta_\pi(\lambda,tr,z_k)=\sum_i \sigma_\pi(tr,\lambda,i,z_k)\frac{\zeta(tr,i,z_k)}{V(i)\rho(tr)}, \tag{22c}$$

where σ_s, σ_e and σ_π are scattering, extinction and backscattering wet-volume cross-sections, V is dry volume for each aerosol size bin i, ζ is mass density for every aerosol component tr and size bin, ρ is dry aerosol density, λ is the wavelength and z_k is the altitude level. Single-scattering albedo (SSA), lidar ratio (S) and optical depth (τ) are obtained from:

$$SSA(\lambda,tr,z_k)=\frac{\beta_s(\lambda,tr,z_k)}{\beta_e(\lambda,tr,z_k)}, \tag{23a}$$

$$S(\lambda,tr,z_k)=\frac{\beta_e(\lambda,tr,z_k)}{\beta_\pi(\lambda,tr,z_k)}, \tag{23b}$$

$$\tau(\lambda,tr)=\sum_k \beta_e(\lambda,tr,z_k)\Delta z_k, \tag{23c}$$

where Δz_k is the thickness of the model layer.

At any altitude in atmosphere, aerosol scattering, extinction and backscatter coefficients are obtained by summation over all aerosol components as

$$\beta_{s,e,\pi}(\lambda,z_k)=\sum_{tr}\beta_{s,e,\pi}(tr,\lambda,z_k). \tag{24}$$

Similarly, the effective values of aerosol *SSA*, lidar ratio and aerosol optical depth are computed by:

$$SSA(\lambda,z_k)=\frac{\beta_s(\lambda,z_k)}{\beta_e(\lambda,z_k)}, \tag{25a}$$

$$S(\lambda,z_k)=\frac{\beta_e(\lambda,z_k)}{\beta_\pi(\lambda,z_k)}, \tag{25b}$$

$$\tau(\lambda)=\sum_k\beta_e(\lambda,z_k)\Delta z_k\ . \tag{25c}$$

Vertical profiles of attenuated backscatter coefficient for all aerosol components as well as for an overall aerosol are calculated, respectively, by:

$$\beta_\pi^A(\lambda,tr,z_k)=\beta_\pi(\lambda,tr,z_k)\sum_{z_k}^{z_{k_{top}}}\exp\left[-2\beta_e(\lambda,tr,z_k)\Delta z_k\right], \tag{26a}$$

$$\beta_\pi^A(\lambda,z_k)=\beta_\pi(\lambda,z_k)\sum_{z_k}^{z_{k_{top}}}\exp\left[-2\beta_e(\lambda,z_k)\Delta z_k\right], \tag{26b}$$

where the term represented by the sum is the two-way attenuation.

Aerosol scattering data included in the Simulator model were derived under the assumption that the aerosol optical properties are not sensitive to the ambient relative humidity. With increasing relative humidity soluble aerosol particles absorb water, the particle size increases, the refractive index changes toward the refractive index of water, and consequently, the aerosol optical properties also change. Treating aerosol as dry in model simulations where atmospheric conditions include significant presence of soluble aerosol can lead to an incorrect estimation of aerosol radiation effects. In order to account for the effects of humidity on aerosol optical properties, new IS aerosol scattering library are established by varying the values of complex refractive index with increasing relative humidity of a wet aerosol. The method used for computing cross-sections is identical to the one followed in computing the look-up tables, while elements of the scattering matrix at high angular

resolution are computed by utilizing Equation (19). The new tables used in the current study account for moisture alterations of optical properties.

CHAPTER III

EXPERIMENTAL SETUP

3.1 APEX-E3 experiment: site description, instrumentation and measurements

The Asian Atmospheric Particle Environment Change Studies – Experiment 3 (APEX-E3) project took place in East-Asia region from March 15 to April 14, 2003. This region is of particular interest due to the large advection of aerosol from China's industrial region and dust from Gobi desert during the spring. The objective of APEX-E3 experiment in view of testing the EarthCARE mission measurements was to measure the aerosol properties and their effects on the cloud system in the East-Asia region (http://157.82.240.167/duckbill/apex/APEX-E3/APEX-E3.plan.v2.2E.pdf).

APEX-E3 observation areas took place within the triangle connecting islands Kagoshima, Amami and Fukue at southwest Japan (Fig. 3.1). In this experiment, the measurements were carried out by a W-band cloud profiling radar and a UV Mie lidar installed on the Gulfstream-2 (G2) aircraft with a beam direction of both instruments set to nadir. The altitude of the G2 measurements varies between 8 and 10 *km*. The line connecting the points 1 to 4 indicated in Fig. 3.1 outlines the G2 measurement area during APEX-E3. A frequency of radar was 95 *GHz* with a minimum detectable reflectivity of -30 *dB* at 5 *km*, while the lidar transmitting wavelength was 355 *nm* and both parallel and perpendicular Mie backscatter components were measured. Table 3.1 summarises the design and performance of these instruments.

In the absence of space-borne EarthCARE measurements, the application of EarthCARE IS to model validation based on radar and lidar measurements will be examined using APEX-E3 G2 observations.

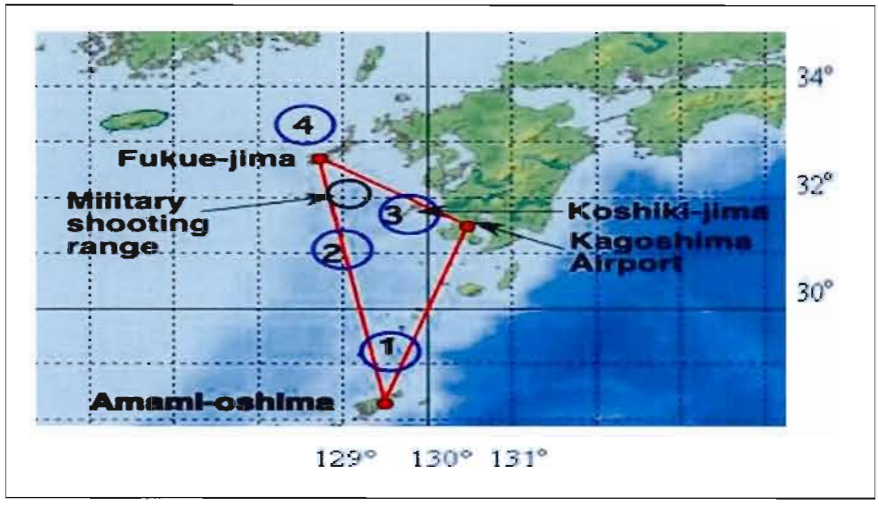

Figure 3.1 The flight path for the APEX-E3 measurements on 27th March 2003. The horizontal and the vertical axes denote the longitude and the latitude respectively.

Table 3.4 Characteristics of APEX-E3 Gulfstream 2 radar and lidar observation systems

G2 max observation height	12 000 m
G2 observation speed	100 – 250 m/s
Beam direction of lidar and radar	nadir
Minimum radar detectable level	-30 dBZ at 5 km
Radar frequency	95.04 dBZ
Lidar frequency	355 nm
Lidar detectable channels	Mie parallel and Mie perpendicular

Fig. 3.2 shows time-height sections of cloud echoes observed by airborne W-band radar and Mie lidar for the selected day for the experiment, March 27, 2003. The upper figure shows radar reflectivity factor in *dBZ* and the lower one lidar's total return signal in *dB*. The

bars at the bottom show periods when the radar and lidar beams were pointed to off-nadir. The G2 airborne flight path corresponding to these measurements is illustrated with the red line at the left corner of Fig. 3.2. Radar and lidar observation segments on March 27 are shown in Table 3.2. The time period of 10:30-12:00 JST (Japan Standard Time) corresponds to airborne observations along the flight path situated approximately at latitudes and longitudes between 129-130° *N* and 31-33° *S*, respectively. The flight report noted the presence of a cirrostratus cloud with base at 5 to 6 *km* and top at 12 *km*. The copy of this report is shown in Appendix A.

Table 3.5 The observation time of APEX-E3 G2 measurements

G2 AIRCRAFT OBSERVATIONS 27 03 2003		
N° of experiment	Time of measurements (JST) (h : min : sec)	Duration (min : sec)
1	10:31:01 - 11:00:29	29:28
2	11:00:32 - 11:13:55	13:23
3	11:14:49 - 11:25:16	10:26
4	11:34:30 - 12:03:54	29:24

3.2 NARCM simulation as input for the EarthCARE Instrument Simulator

Following the APEX-E3 aircrafts campaign, NARCM was applied to simulate the synoptic condition at that time. The analysis of the aerosol properties and their effects on the cloud system in Eastern-Asia are investigated during this period. The NARCM simulation done by Rodrigo Munoz-Alpizar (article in preparation) captures the main features of the 3-D structure, the size distribution and the composition of observed aerosol. The output of this simulation is employed as input for the EarthCARE Instrument Simulator in order to evaluate

the fields of radar reflectivity and lidar backscattering from NARCM-simulated corresponding cloud system.

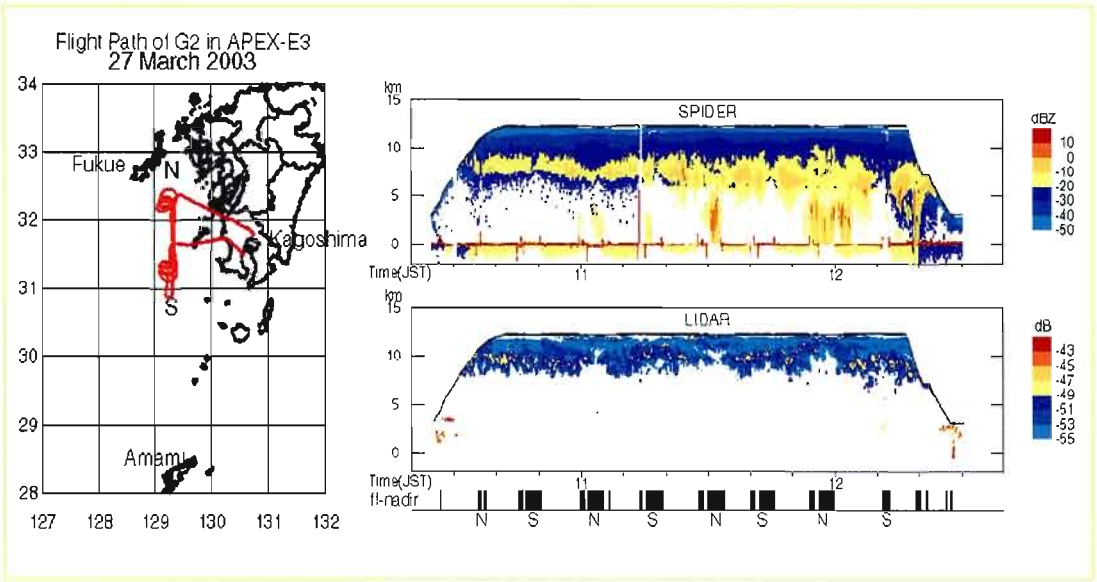

Figure 3.2 Time-height sections of cloud echoes observed by airborne W-band radar and Mie lidar of the selected day for the experiment, March 27, 2003. Radar reflectivity factor in *dBZ* (top right) and lidar's total return signal in *dB* (bottom right). The bars at the bottom show periods when the radar and lidar beams were pointed to the off-nadir. The G2 airborne flight path corresponding to these measurements is illustrated with the red line at the left panel.

NARCM is driven by the reanalysis from European Centre for Medium-Range Weather Forecasting (ECMWF) using ERA-40 data for spring 2003 at 0.4×0.4 degree. The model is initialized on 15.03.2003 at 00:00 GMT (Greenwich Mean Time) and driven using the ECMWF wind speed, temperature and relative humidity updated every 6 hours. The simulation is performed with the horizontal resolution of 45 *km*, 22 vertical levels and a time step of 900 seconds. The NARCM 45-km domain covers the East Asia region including the western end of Japan near northern East Asia as well as parts of China and Korea (Fig. 3.3).

The analyses of this simulation have shown that simulated cloud system for March 27, 2003 corresponds approximately to the observed cirrostratus. In this study, microphysical characteristics of the NARCM simulated cloud system are converted into radar reflectivity

factor and lidar backscattering via EarthCARE Instrument Simulator and compared with the observed APEX-E3 G2 radar and lidar measurements.

a)

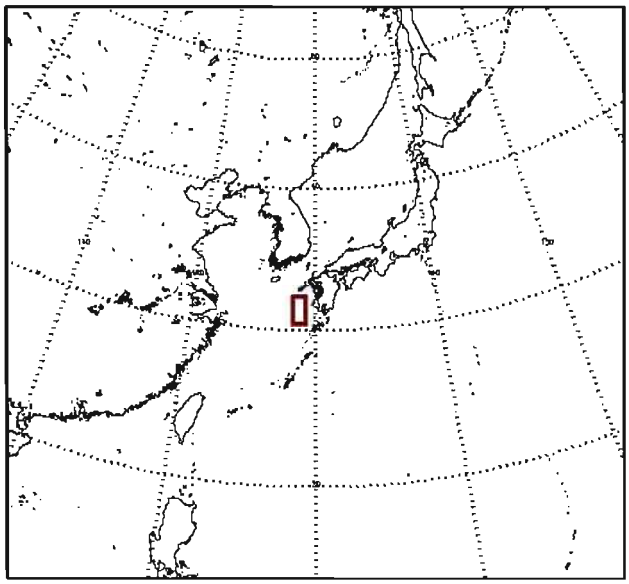

b)

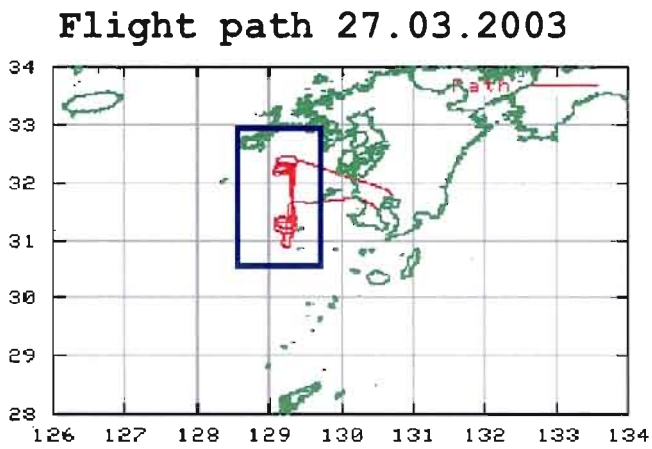

Figure 3.3 a) Domain of the driving low-resolution NARCM simulation. The brown square denotes the domain of the high-resolution nested NARCM simulation used to validate the model. The smaller domain is magnified in (b).

The airborne-G2 radar and lidar measurements are performed between 10:30 and 12:00 JST at the vicinity of Kagoshima (131.1°E, 31.2°N), Amami (128.5°E, 28.4°N), and Fukue (128.7°E, 32.8°N) islands. The frequency of the radar and lidar profile-measurements was approximately three per seconds during the observation period. The observation area and the time duration of airborne G2 measurements correspond to a region of 2×5-grid points and to 3 sampling times (one per hour) in the NARCM-45 km domain. The large difference in spatiotemporal resolution between the simulation and observations implies that only a comparison of average values is possible. Therefore, the mean and the standard deviation profiles of a random variable $\xi_{k,i}$, $\overline{\xi_k}$ and SD_k, respectively, are computed as follows:

$$\overline{\xi_k} = \frac{1}{N_{i,\,\xi\neq 0}} \sum_{i}^{N_i} \xi_{k,i}\,, \tag{27}$$

$$SD_k = \sqrt{\frac{1}{N_{i,\,\xi\neq 0}} \sum_{i,\xi\neq 0}^{N_i} \left(\xi_{k,i} - \overline{\xi_k}\right)^2}\,, \tag{28}$$

where $N_{i,\xi\neq 0}$ is the vertically dependent number of samples. The indices k and i denote the vertical position and the sample size (the number of grid-point multiplied by the number of sampling times), respectively.

CHAPTER IV

RESULTS AND DISCUSSION

4.1 NARCM water content and temperature

Average and standard deviation profiles of NARCM ice and liquid water content (IWC and LWC, respectively) are shown in Fig. 4.1 (left panel). Also shown in Fig. 4.1 are numbers of samples taken for computing the statistics (right panel). The number of samples, which is a function of height, illustrates the number of horizontal levels at which some IWC (LWC) values occur (in relation to total number of grid-points). Standard deviation profiles show the spread of the data around the mean values. A significant amount of ice water content is present on altitude-levels between 6 and 12 *km* with maximum values of 0.014 ± 0.005 grm^{-3} around 9 *km*. Although IWC is present at altitudes below about 6 *km*, its values are not larger than 10^{-3} grm^{-3}. Liquid water content is present at almost all altitudes with two significant local maxima, one of 0.14 grm^{-3} around 5.5 *km* and a second one of 0.04 grm^{-3} between 8 and 9 *km*. Its standard deviation profile is skewed right (toward higher values of liquid water content). Thus, at any specific altitude level, LWC values are widely spread around the mean such that at 5.5 *km* local maximum varies in the range of approximately 0.04 – 0.4 grm^{-3}. Also, it can be seen that at all altitudes where ice appears, a significant amount of water is present. It is worth nothing that the region where the local, upper LWC maximum is placed is exactly below altitude-levels where maximal values of IWC occur.

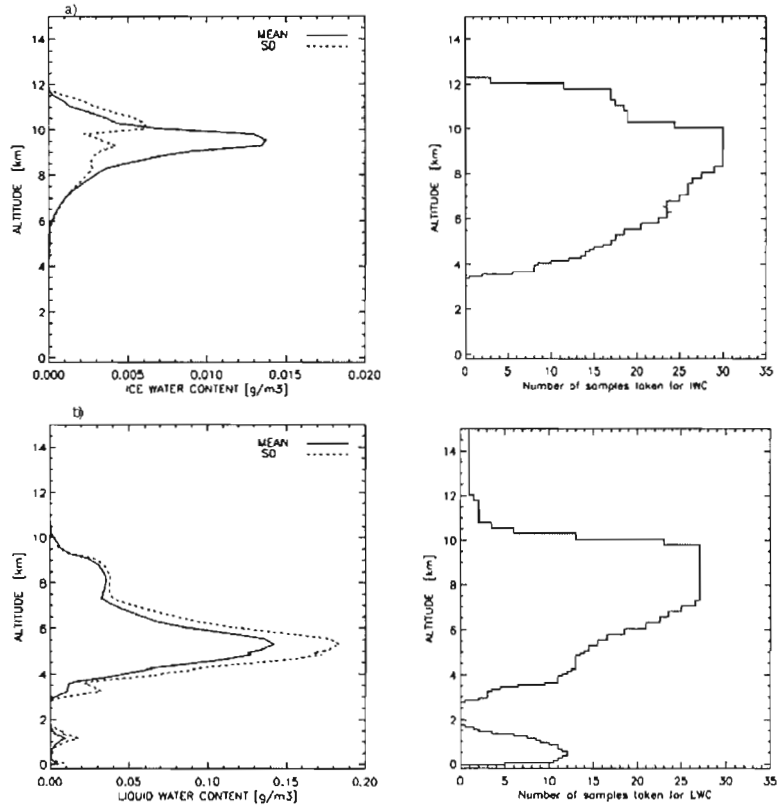

Figure 4.1 NARCM water content profiles in *gm-3*. The panels on the left show the mean (*full line*) and the standard deviation (*dotted line*) vertical profiles of: *(a)* ice-water content and *(b)* liquid-water are shown on left panels. The panels on the right-hand side show the number of the model grid points used to compute the statistics.

In Fig. 4.2 the vertical profile of the average temperature at its standard deviation range is compared against the observed one. It is important to note that temperature drops below $0°C$ at approximately 3 *km* altitude-level, which implies the presence of supper-cooled water at all higher levels (see profile of LWC in Fig. 4.1b). It can be seen that the two temperature profiles are not identical: the difference is minimal around 5 *km*, but increases with altitude to values as high as 10 degrees between 8 and 9 *km* and decreases above. Such a large discrepancy between the modelled and the observed temperature can induce considerable differences in the simulated cloud microphysical properties. The threshold temperature for

homogenous freezing set at –35°*C* in the NARCM simulation is reached at 10 *km* and above. On the other hand, if the modelled and the observed temperature profiles were identical, this threshold would be reached at 8.5 *km*, which implies that NARCM-simulated IWC (LWC) is underestimated (overestimated) at altitudes between 8.5 and 10 km. The same argument holds for levels below 8.5 *km* since the NARCM-simulated temperature at these altitudes is also higher relative to the observations, which decreases the heterogeneous freezing rate.

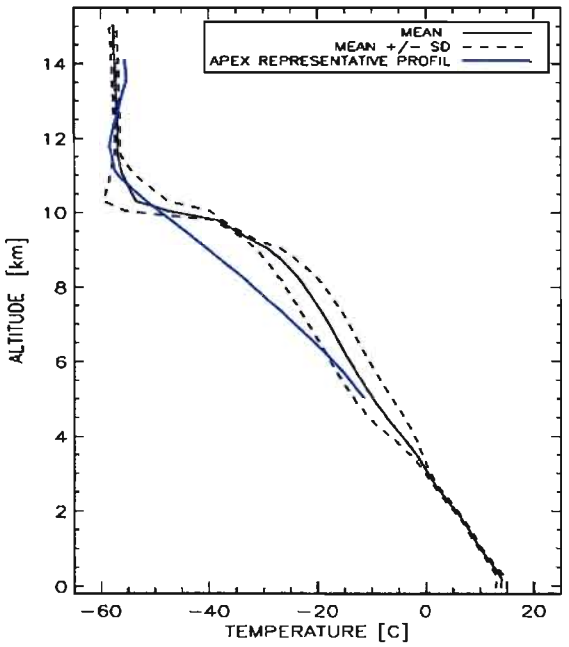

Figure 4.2 Mean NARCM temperature vertical profile against the one observed.

The standard deviation of the NARCM-simulated temperature, shown in Fig. 4.2, varies from 0 to 5°*C*. It is interesting to note that the standard deviation is approximately zero at altitudes between 9 and 10 *km*, where the homogeneous threshold is reached in the NARCM simulation. This implies that this threshold is reached at the same level at all considered grid points; there is no NARCM grid point with a temperature profile closer to the

observed average profile at the level critical for the homogeneous nucleation. Furthermore, inspection of the IWC vertical profile (shown in Fig. 4.1) shows that it is exactly at these levels where the NARCM-simulated IWC reaches its maximal values.

Profiles of IWC and LWC in Fig. 4.1 indicate a presence of a deep cloud layer between about 4 and 12 *km*, which mostly part consists of ice at altitudes above 10 *km*, and of super-cooled water in addition to ice above 6 *km*. It is important to note that the vertical extent of the modelled cloud corresponds well to the width of the observed one indicating that the model captures the synoptic scale structure of the observed cloud.

4.2 NARCM aerosol

The vertical profiles of a mean aerosol mass concentration from NARCM are shown in Fig. 4.3. The average "total" aerosol profile is acquired by summation over all size-bins and species from NARCM aerosol components at each vertical column (orange line in Fig. 4.3). These vertical profiles for sulphate, dust, organics and black carbon show a similar pattern. An inspection of Fig. 4.3 shows the existence of two local maxima: very large one in the lower troposphere around 3.5 *km*, and another, smaller one, centred at 10 *km*. It is important to note that a difference between these maxima is approximately two orders of magnitude but varies considerably in term of aerosol types. Furthermore, it can be seen that altitude-levels corresponding to the upper aerosol maximum are also the levels where maximal values of ice water content are located (Equation 15). At altitudes where LWC reaches its maximum there is no indication of significant aerosol mass concentration, except for some sea-salt layer around 6 *km*. The aerosol layer mainly composed of sulphate at altitude around 3.5 *km*, is localized just below the level of higher LWC maximum.

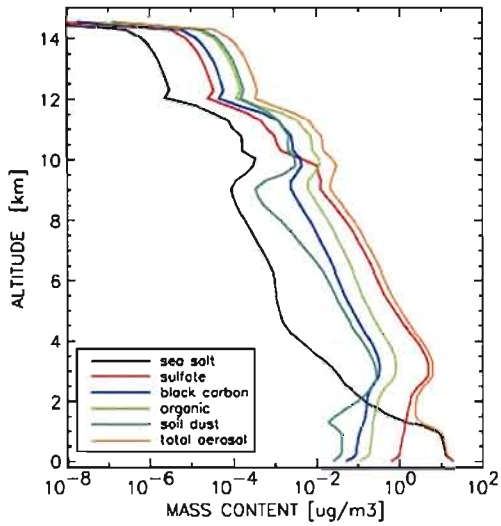

Figure 4.3 Variation of the average mass concentration of NARCM aerosol components with height.

The sea-salt vertical profile is different from those of other aerosol. Large sea-salt mass concentration values in the lowest troposphere result from the emission by the ocean surface. It is important to note that below 2 *km* the total aerosol mass concentration is mainly composed of sea-salt. A local maximum of about 10 μgm^{-3} is found around 1 *km*. There, the sulphate concentration is about one order of magnitude lower than that of sea-salt while the concentrations of other aerosol components are not significant. At altitudes above 2 *km*, sea-salt mass concentration strongly decreases with height but reaches two additional local maxima, both within the altitude-regions of LWC and IWC maxima, around 6 and 10 *km*, respectively. While the maximum at 6 *km* is manifested through a slight convex enhancement, the sea salt mass concentration entirely follows the shape of mass concentration of other aerosol types within the IWC region, reaching a value of 10^{-4} μgm^{-3}, which is five time less than at 6 *km*.

For aerosol components other than sea-salt, of big importance is the region around 3.5 *km* where the average total aerosol mass concentration reaches maximal values of about 10 μgm^{-3}. The layer with maximal concentration is confined between the ocean surface and

approximately 5 *km*. The analysis indicates that this layer was primarily due to the advection of aerosol mass from China (not shown here). As it can be seen in Fig. 4.3, the maximum at 3.5 *km* is mainly composed of sulphate aerosol, most likely anthropogenic. A contribution of organic carbon is smaller than that of sulphates by at least one order of magnitude, and in the case of other aerosol, even smaller. Sulphate mass concentration dominates over mass concentration of other aerosol components at altitudes up to 10 *km* above which it decreases, reaching values even less than those of dust, organic and black carbon. Consequently, a contribution of the aerosol types in achieving of the local maximum value at 10 *km* is quite different than the composition found in the lower troposphere.

It is worthy to mention that soil dust profile differ from the uniform vertical distributions of other aerosol types. At altitude-levels above 10 *km* dust mass concentration is larger than that of sulphates, but still smaller than organic and black carbon.

Average number and mass distributions of "total" aerosol at different altitudes are shown in Figs. 4.4a and 4.4b respectively. On both figures, horizontal axis represents the particle radius plotted on a logarithmic scale. Different colours of the curves represent the average distribution profiles on specified altitude levels. Overall, a gradual decrease in number and mass distribution occurs with increasing altitudes while its shape remains similar. Broadly speaking, aerosol is characterized with a tri-modal distribution ranging from the nucleation mode (less than 0.02 μm), to the accumulation mode (between 0.02 and 0.08 μm) and to the giant mode (centred at 1 μm). It is remarkable to note that the large number of particles near 0.01 μm in radius implies a recent nucleation event. It is important to notice that, near the surface, the mass distribution of the micron-size particles is larger than that of the accumulation mode, and still remains remarkable even though it slightly decreases with altitude.

A high concentration of Aitken particles at 3.5 *km* (blue line) around 1000 cm^{-3} as well as a considerable number of micron-sizes particles indicate that aerosol layer in lower atmosphere is mainly due to advection of particles recently formed from gas-to-particle conversion and older ones advected in the accumulation mode.

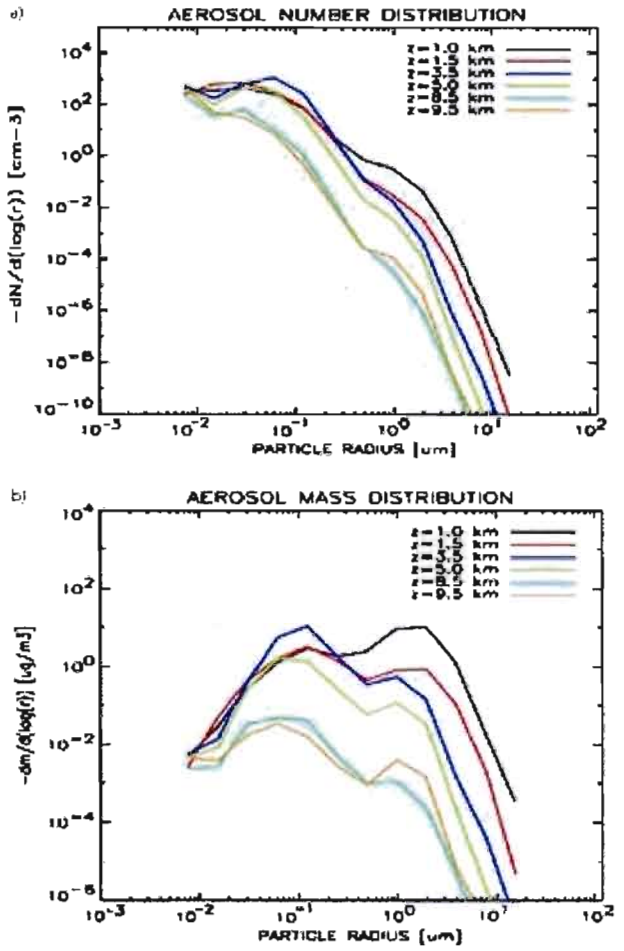

Figure 4.4 Variation of the average number distribution (a) and average mass distribution (b) of "total" aerosol with height.

It is important to note that distributions near 9.5 *km* and within the region of ice cloud show a relative increase of aerosol toward the radii of few micrometers (orange line, Figs. 4.4a and 4.4b).

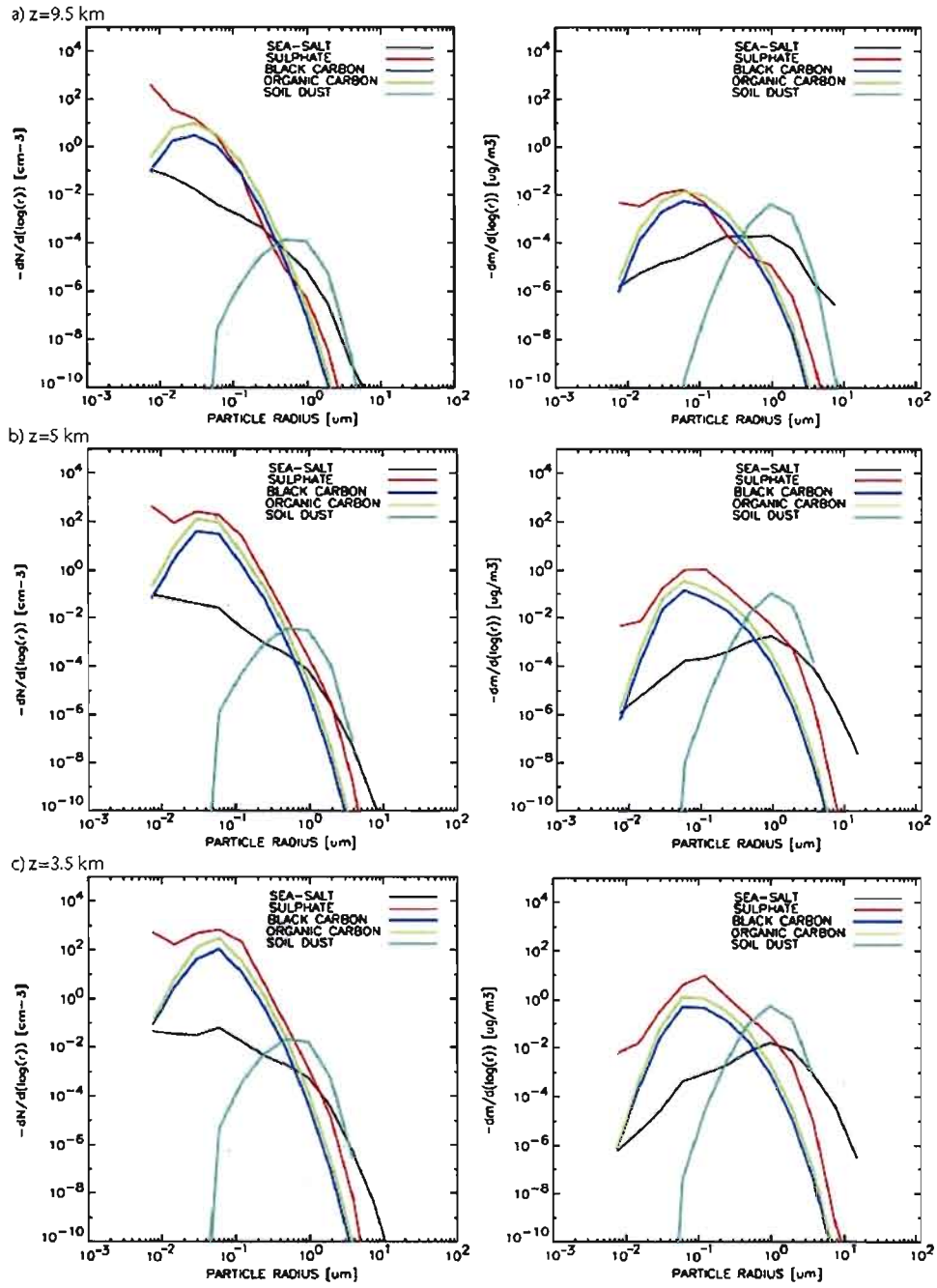

Figure 4.5 Average number (left panel) and mass distribution (right panel) of NARCM aerosol components at altitude levels characterized with: a) max IWC, b) max LWC and c) max total aerosol mass concentration.

Average number and mass distributions for each aerosol component at three altitude levels are shown in Fig. 4.5. Chosen levels correspond to altitudes where maximum values of ice water content (Fig. 4.5a), liquid water content (Fig. 4.5b) and aerosol mass concentration (Fig. 4.5c) are located, respectively. Fig. 4.5a shows the location of the dominant maxima of large (microns) particles at 9.5 *km* altitude. It is dominated by soil dust and sea-salt particles. Similarly, near the LWC maximum (Fig. 4.5b), in addition to sea-salt and dust, there is a significant amount of large sulphate particles. An inspection of Fig. 4.5 shows that shapes of distribution curves, mostly of sea-salt and soil dust remain similar with altitude. However, the appearance of these particles at high altitudes, as well as the preservation of its size distributions with large particles implies that the model had relatively strong vertical velocity in the region causing air mass to be well mixed deeply in the troposphere. Black carbon and organics mantain their size distributions with altitude, and the same can be said for soil dust and sea-salt. However, the absolute amplitude of these distributions changes substantially, except at altitudes near 9.5 *km* where IWC maximum is located. There, distribution peaks belonging large mode are stronger than around 8.5 *km* (see Fig. 4.4). An analysis showed that primary dust and sea-salt are responsible for this situation: their distributions belonging to the large particle suddenly increase after a local minimum at 9 *km*, while in the case of other aerosol components, an increase in mass concentration is due to an increase of Aitken particles.

However, the most interesting is behaviour of sulphate distributions. The increased concentration of Aitken particles as well as the nucleation mode gives evidence that a significant amount of the sulphate particle load is formed by chemical reactions most likely in-cloud oxidation (Van Salzen *et al.*, 2000). By comparing sulphate mass distribution curves (red curve in Figs. 4.5a and 4.5b, right panel) it can be seen that size distributions between two dominant modes is reduced in concentration at altitudes where ice is present. The sulphate removal is partly due to their activation as CCN. This behaviour is not noticed in the case of other aerosol components as a consequence of parameterizations used in Lohmann microphysics scheme based on sulphate.

It is important to mention that a strong advection of anthropogenic aerosol from China and Korea was reported in the period of March 25-27, 2003 (Takami *et al.*, 2005; Mukai *et*

al., 2005). The transport of aerosol, described as "no dust event", was characterised with unusually high sulphate loading. Takami reports that observed high concentration of an internally mixed aerosol was associated with high sulphate, ammonium and "organic" aerosol ("organic" in this category represents aerosol primarily made of carbon, oxygen, hydrogen and nitrogen molecules) loading whose size distributions consisted of mostly the accumulation mode particles. Similar report was obtained from aircraft measurements at the altitude levels 1-3 *km* (Bahreini et al., 2003).

It is worth noting that large particles (1-2 μm) made of elemental carbon, dust and sea-salt aerosol were not measured during this experiment. However, lidar measurements of Asian dust at the APEX-E3 measurement area indicate that the dust particles are mixed with other pollutant gases at the same altitude range (Lee C.H. *et al.*, 2004). Takami suggested that high mass concentration of measured nitrates could be related to the nitrate internally mixed with dust or sea-salt particles. Also, the flight report for March 27 noted elevated black carbon concentration at high altitudes.

4.3 Effective radius and number concentration

As it has been mentioned before, aerosol and cloud bin number distributions serve as input for lidar and radar instrument modules. The NARCM simulated liquid (ice) water content is expressed as size-distributions of the equivalent (volume) radius that are assessed by assuming a modified-gamma distribution for given radius ranges. Variation of the mean effective radius and of the corresponding total number concentration of cloud droplets with altitude is shown in Figs. 4.6a and 4.6b, respectively. Here, the total number distribution is obtained by summation of the number distributions over different radius ranges.

Layer up to 2 *km* altitude is characterized by effective radius below 2 microns, small number concentration with a maximum of 300 cm^{-3} and low water content (less than 0.01 $g\ m^{-3}$). According to various observations, these values are typical for fogs (Pruppacher and Klett, 1978). Maximal values of droplet concentration of 700 to 800 cm^{-3} at altitudes between 3 and 4 *km* are related to a relatively small value of droplet effective radius (2 microns). The

total number concentration decreases with altitude from 800 to less than 100 cm^{-3} around 10 *km*. The droplet effective radius has two important local maxima, one of 5 microns below 6 *km* and another of 6 microns below 9 *km*. As seen in Fig. 4.1b, maximum values of droplet effective radius correspond to maximum values in water content.

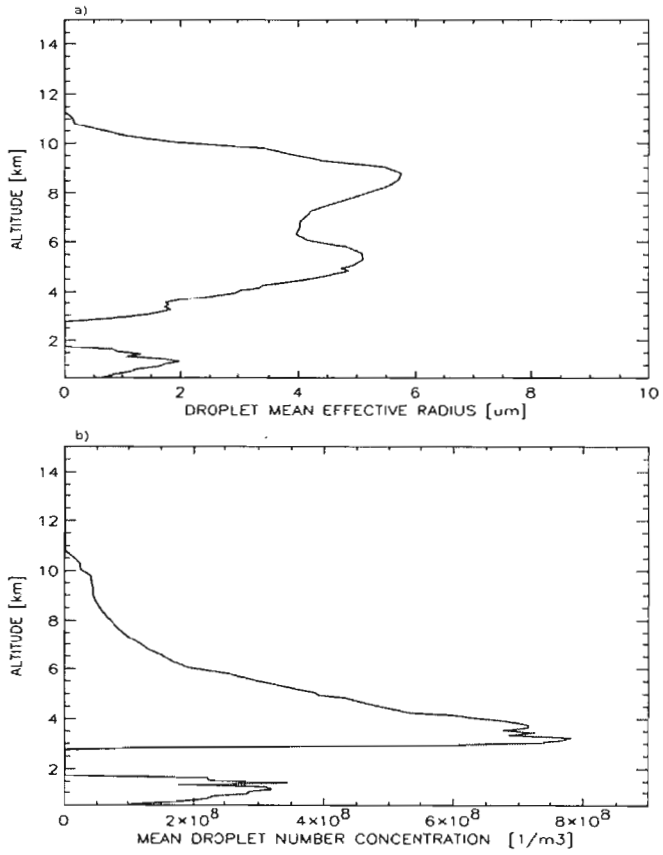

Figure 4.6 Mean vertical profiles of a) droplet effective radius and b) number concentration.

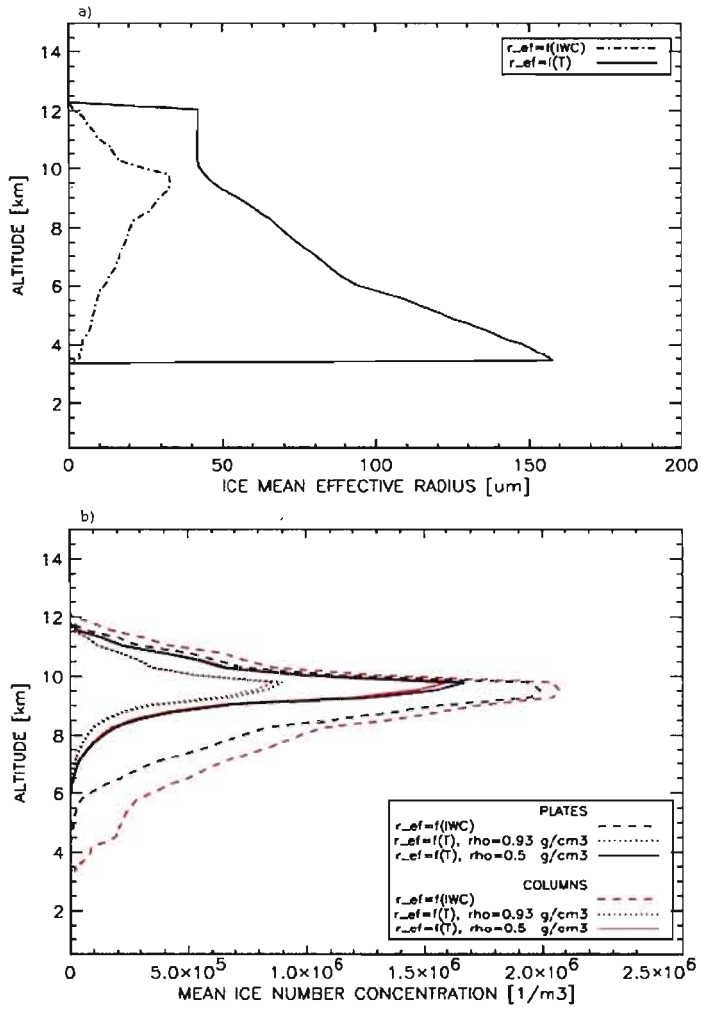

Figure 4.7 Mean vertical profiles of a) ice effective radius and b) number concentration obtained by varying the shape and density of ice particles.

Concerning the ice phase cloud, two experiments are performed. In the first experiment, the effective radius for ice phase is expressed as function of IWC (Lohmann and Roeckner, 1996) while in second, as a function of the temperature (Lohmann, 2002) (Equations (16) and (17), respectively). The vertical profiles of effective radius computed following these methods are shown in Fig. 4.7a. Recall that in the first of these methods the effective radius is parameterized according to an empirical relationship with the ice crystal

distribution and the observed ice water in frontal clouds, while in the second, it is expressed as a function of the temperature based on the observations from mid-latitude cirrus. Fig. 4.7a shows that the values of the effective radius computed as a function of temperature are, at all altitudes, larger than in the case when they are computed from the formulation of Lohmann and Roeckner (1996). The distinction between two profiles is smallest below 10 *km*, where the IWC maximum is located.

Radiative properties of ice clouds are usually parameterized as a function of water content and the particle effective size. The effective radius of ice particles highly depends on their habits and distributions. Both parameterizations of effective radius used in this study, as based on observations, allow that ice cloud may be composed of differently shaped particles. In situ observations and studies indicate that cirrus are composed of columns and likely bullet rosettes and plates (Knollenberg, 1970; Heymsfield and Platt, 1984; Liou, 1992). In further analysis we suppose that ice particles could be either columns or plates. This assumption is involved by specifying the different size-ranges for columns and plates when applying the modified-gamma distribution. The bin-size grids for columns and plates used to compute the number density concentrations are shown in Table 4.1.

Radiative properties of ice clouds are usually parameterized as a function of water content and the particle effective size. The effective radius of ice particles highly depends on their habits and distributions. Both parameterizations of effective radius used in this study, as based on observations, allow that ice cloud may be composed of differently shaped particles. In situ observations and studies indicate that cirrus are composed of columns and likely bullet rosettes and plates (Knollenberg, 1970; Heymsfield and Platt, 1984; Liou, 1992). In further analysis we suppose that ice particles could be either columns or plates. This assumption is involved by specifying the different size-ranges for columns and plates when applying the modified-gamma distribution. The bin-size grids for columns and plates used to compute the number density concentrations are shown in Table 4.1.

Table 4.6 Bin-size grids of columns and plates used in computing the number density distributions

Columns bin-diameter (μm)	Plates bin-diameter (μm)
1.75	15
5	30
15	65
30	150
65	300
150	650
300	-
650	-

Ice clouds are composed of particles having different shape, sizes and bulk densities. Bulk density may change during the transition processes between different types of ice crystals and as thus, it is a function of temperature and super-saturation. Recently, several studies investigated the effect of bulk density on retrievals of ice microphysical parameters by using microwave frequencies (Matrosov *et al.*, 1996; Ryzhkov *et al.*, 1998; Weng and Grody, 2000). For example, some of the reported ice bulk densities may be as low as 0.1 $g\ cm^{-3}$ for snow, 0.13 $g\ cm^{-3}$ for small graupels, 0.5 $g\ cm^{-3}$ for graupels and needles, 0.6 $g\ cm^{-3}$ for spongy ice and 0.916 $g\ cm^{-3}$ for solid ice, hexagonal plates and solid thick plates. However, these density values for specified types may vary, as the natural ice is a complex structure of solid ice and air. An excellent summary of reported assumptions on the shape and density of ice particles in function of their size is given by Matrosov *et al.* (1996). These mass-size relations are commonly used in recent studies when investigating the microphysical properties of ice clouds.

In the formulation of modified-gamma distribution, described in Section 1.3, it can be seen that the distribution characteristic size (Equations (12) and (13)) depends not only on the

water content and the effective radius but also on the hydrometeor bulk density (through the parameter $\bar{\xi}$ in Equation (12)). The bulk density of ice particles used in NARCM is 0.916 $g\ cm^{-3}$. For the NARCM simulated IWC and effective radius obtained as a function of IWC, it is correct only to use the solid ice density. But the effective radius parameterization in a function of temperature (Lohmann, 2002) does not depend on ice water content, and may be attributed to various ice densities. Lohmann (2002) used a value of 0.5 $g\ cm^{-3}$ for bulk density of ice crystals. In this study, we examine two cases when applying Lohmann (2002) parameterization for effective radius. In the first case we assume that ice density is 0.916 $g\ cm^{-3}$ while in second, 0.5 $g\ cm^{-3}$.

Variation of the vertical profiles of the average total number concentration of ice particles with respect to different assumptions regarding their shape and bulk density is shown in Fig. 4.7b. In spite of the large distinction between vertical profiles of ice effective radius with altitude of maxima, the number concentration profiles have their maxima at the same level below 10 *km*. Furthermore; this is also the altitude at which ice water content achieves its maximum. It can be seen that the choice of ice effective radius parameterization has a considerable influence in distributions of ice particles. There is a large number of small ice particles in the case of the frontal clouds parameterisation and a small concentration of large ice in the case of the cirrus-temperature parameterization. Bulk density fluctuations have also a considerable influence. A decrease of ice density produces an increase in ice number concentration (see Fig. 4.7b, dotted and full lines). This behaviour is pronounced at altitudes where total number concentrations attain their maximum.

As seen from Fig. 4.7b, it seems that the total number concentration is not sensitive to variations in particle shape (column and plate). The only exception is a distinction that appears in the case of frontal clouds parameterization at lower altitudes and is caused by the fact that the representative mod-radii for column and plates differ, especially in the lowest radius-range.

4.4 Radar reflectivity and backscattering coefficient

A number of studies have been addressed to find the empirical relation between the radar reflectivity factor and liquid (ice) water content. This relation allows for retrieving of the LWC (IWC) from given radar measurements. Some of the empirical formulas have been found for stratocumulus and non-precipitating cumulus, from sources listed in Table 4.2. Table 4.3 compiles the empirical formula for millimeter-wave radar and cirrus cloud considered in this study. A universal relation between the radar reflectivity factor (RRF) and the liquid (ice)-water content does not exist. Due to natural variability of cloud droplet spectra, the empirical formulae from particular case studies cannot be generalized. So, for any given case these empirical relations are not able to reproduce accurately the LWC (IWC) from the measured RRF.

In order to verify our estimation of the RRF based on the assumption of the modified-gamma distribution for the number concentration of the cloud droplets, the empirical relations presented in Tables 4.2 and 4.3 are inverted and the corresponding average RRF vertical profiles are computed from NARCM liquid and ice water content (labelled as "empirical LWC-RRF" and "empirical IWC-RRF" respectively in following discussion).

Mean empirical IWC-RRF and LWC-RRF vertical profiles retrieved from NARCM are shown in Figs. 4.8a and 4.8b, respectively. According to radar reflectivity, the ice cloud is located at altitudes between 6 and 11.5 *km* with a maximum occurring at a level where the peak in ice water content appears, near 9.5 *km*. As seen in Fig. 4.8a, there is a good agreement between different empirical IWC-RRF relations with respect to the top and centre of the ice cloud, but less so for the cloud base. The empirical IWC-RRF maxima vary from –18 to –11 *dBZ* at 9.5 *km*, depending on the chosen empirical relation. An inspection of Fig. 4.1a shows that ice is present at altitudes below 6 *km* but in quantities less than 10^{-3} gm^{-3}. It follows that values of ice water content below this limit are not significant in terms of radar reflectivity because they produce RRF smaller than -40 *dBZ* and are hardly detectable by radar.

Table 4.7 Empirical relations between radar reflectivity and liquid water content considered in this study

Reference	*Empirical relation*
Atlas (1954)	$LWC = 4.56\ Z^{0.5}$
Sauvageot and Omar (1987)	$LWC = 5.32\ Z^{0.55}$
Fox and Illingworth (1997)	$LWC = 9.26\ Z^{0.64}$

Table 4.8 Empirical relations between radar reflectivity and ice water content considered in this study

Reference	Empirical relation
Atlas et al. (1995)	$IWC = 0.64\ Z^{0.58}$
Brown et al. (1995)	$IWC = 0.153\ Z^{0.74}$
Schneider and Stephans (1995)	$IWC = 0.097\ Z^{0.696}$
Aydin and Tang (1997)	$IWC = 0.104\ Z^{0.483}$
Liu and Illingworth (2000)	$IWC = 0.137\ Z^{0.643}$
Matrosov (2002)	$IWC = 0.110\ Z^{0.63}$

Mean empirical LWC-RRF profiles (Fig. 4.8b) show a cloud containing liquid droplets located between 4 *km* and 9 *km* altitude. Two peaks of the radar reflectivity are found at altitudes where LWC maxima occur. Dissimilarities related to different empirical LWC-RRF estimations are mostly in the upper part of the cloud, but, on average, the difference between them is less than 5 *dBZ*. It is important to note that the simulated fog layer below 2 *km* altitude (Fig. 4.1) is not detectable by the radar due to lack of sensitivity.

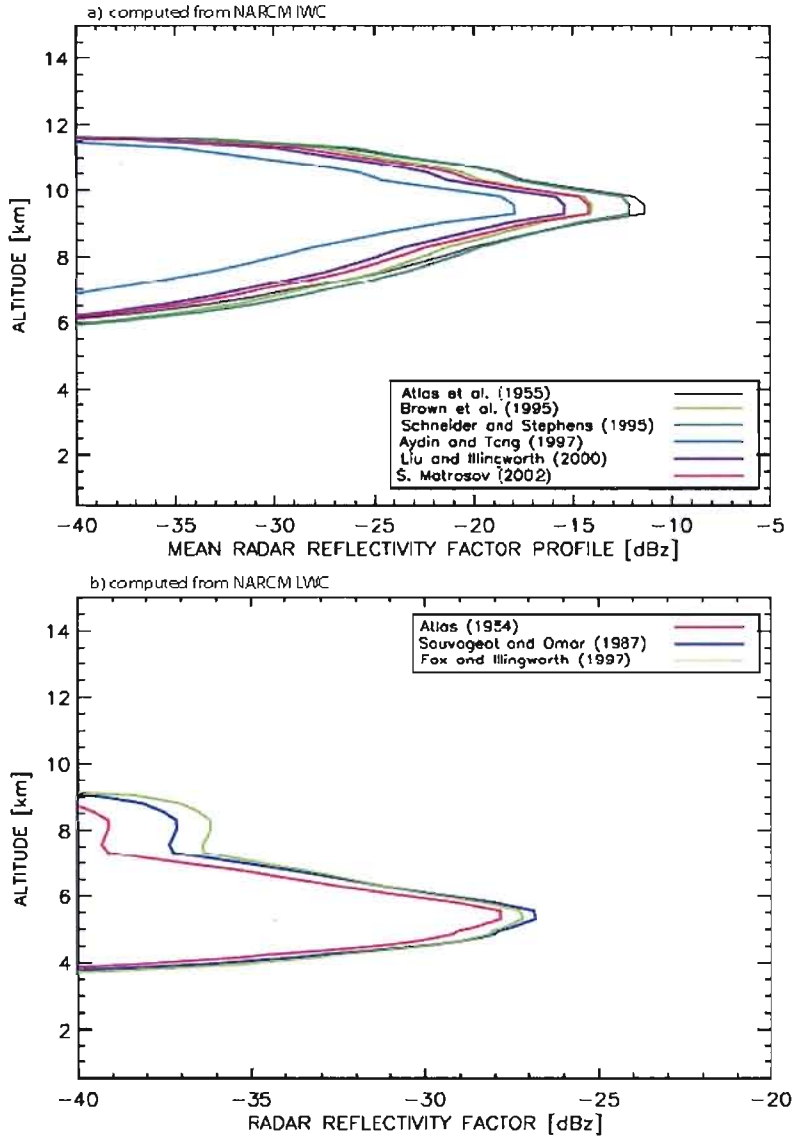

Figure 4.8 Average vertical profiles of radar reflectivity estimated from NARCM IWC (a) and NARCM LWC (b) using empirical formulas from different authors.

Here, NARCM model is used to generate cloud microphysical data fields that are converted into RRF to assess the potential of the cloud validation in the regional climate model from space-borne cloud radar measurements. Instead of the empirical formulae obtained from independent studies (Tables 4.2 and 4.3), the EarthCARE IS requires an

explicit size distribution of droplets and ice crystals. They are not available in NARCM. The simulated NARCM liquid and ice water content are expressed as size-distributions of the equivalent radius (Figs. 4.6a and 4.7a) and assuming a modified-gamma distribution with a given size-ranges. They are converted to the radar reflectivity by the theoretical equation:

$$Z = \int n(D)D^6 dD, \tag{29}$$

where Z represents radar reflectivity factor in mm^6m^{-3}, D is the diameter of cloud particles expressed in *mm* (equivalent diameter for ice) and $n(D)dD$ represents the number of particles having a diameter in the radius interval between $D-dD/2$ and $D+dD/2$ per unit of air volume (m^{-3}). The vertical profiles of total number concentration obtained by this integration are shown in Figs. 4.6b and 4.7b. The reflectivity factor from Equation 29 is converted into decibels (*dBZ*) by:

$$RRF \equiv Z(dBZ) = 10\log(Z(mm^6m^{-3})). \tag{30}$$

The estimation of the RRF based on the assumption of the modified-gamma distribution for cloud droplets and ice crystals are compared against independent results obtained in Fig. 4.8 from empirical relations in Tables 4.2 and 4.3 (Figs. 4.9a and 4.10a). Radar reflectivity profiles determined from NARCM liquid and ice water contents are labelled as "LWC-RRF" and "IWC-RRF", respectively.

In Fig. 4.9a, the LWC-RRF profile (black line) is compared against the RRF profile obtained by averaging all empirically estimated LWC-RRF profiles shown in Fig. 4.8b (blue line in Fig. 4.9a). It can be seen that in the lower part of the cloud, near 6 *km*, the LWC-RRF values are smaller than average reflectivity of the empirical LWC-RRF estimations. In the upper part of the cloud, this situation is opposite: values of LWC-RRF are smaller than the averages determined from empirical LWC-RRF estimations. However, the maximal difference between two profiles is not larger than 3 *dBZ*, and it follows that computed bin-number distributions represent an acceptable input for the Simulator Radar Module.

The EarthCARE simulated reflectivity of liquid cloud (EC-LWC-RRF) is shown in Fig. 4.9b (red line) along with the mean empirical LWC-RRF profile. Simulated EC-LWC-RRF values are very low (-40 *dBZ*) and barely detectable near 9 *km*. They are below the

detectable level of -35 *dBZ* for the EarthCARE radar. Thus, the NARCM simulated LWC does not contribute to the APEX observed reflectivity shown in Fig. 3.2.

Now, we return our attention to the ice cloud. As it was mentioned earlier in this section, the simulated NARCM ice water content is expressed as size-distributions for given size-ranges using a modified-gamma distribution and by specifying the effective radius. The effective radius is computed by two different methods: as a function of IWC (Lohmann and Roeckner, 1996) and as a function of the temperature (Lohmann, 2002). The average vertical profiles of effective radius computed following to these methods are discussed in Section 4.3 and shown in Fig. 4.7a. A distinction between columns and plates is involved by specifying the different size-ranges when applying the modified-gamma distribution. A procedure including the bulk-density variations is described in Section 4.3.

Several vertical profiles of the mean total number concentrations of ice particles obtained under different assumptions regarding their effective radius, shape and density are shown in Fig. 4.7b. Number density concentrations corresponding to these cases are used in computing the radar reflectivity (Equations (29) and (30)). These reflectivity values are averaged following Equation (27) for each case of assumed microphysical properties for ice cloud. The average IWC-RRF profiles computed following this procedure are shown in Fig 4.10a (black and red lines).

As seen on Fig. 4.10a, columns shaped ice particles have greater RRF values than plates. Also, it can be seen that ice particles with a lower density (and higher number concentration (Fig. 4.7b)) have larger RRF values than those with a greater density value (and lower number concentration (Fig. 4.7b)).

Also, in Fig 4.10a, the IWC-RRF profiles are compared against the RRF profile resulting from averaging all independently estimated IWC-RRF profiles (Fig. 4.8a) from empirical relations shown in Table 4.3. Recall that this comparison verifies our estimation of the RRF based on the assumption of the modified-gamma distribution for the number concentration as well as of the ice cloud microphysical properties (shape, effective radius and bulk density).

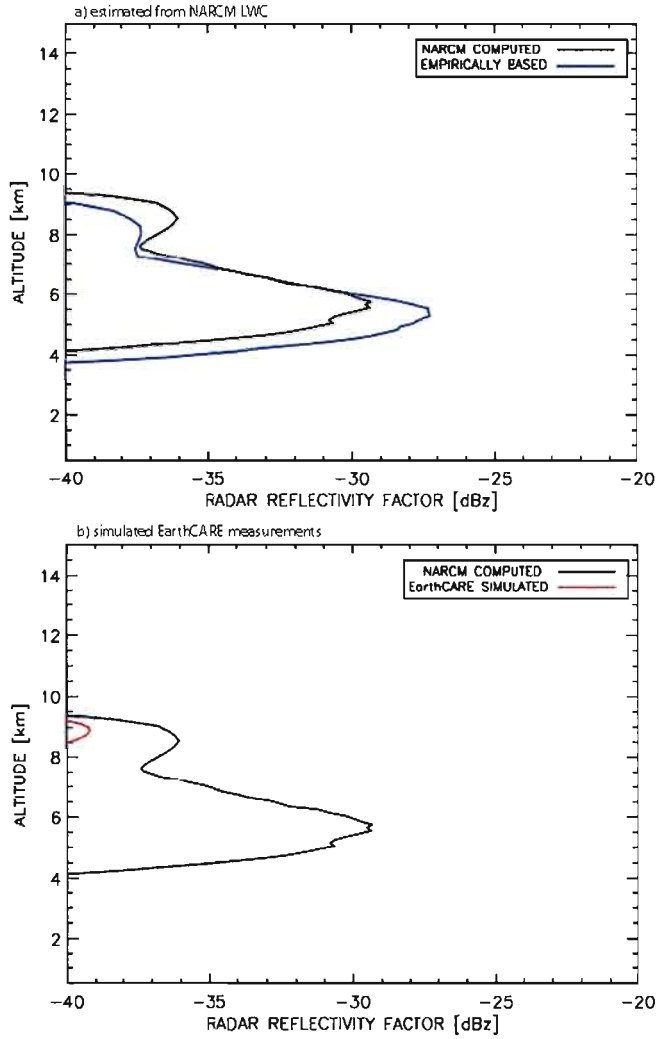

Figure 4.9 Mean radar reflectivity profiles assuming liquid phase only present a) LWC-RRF computed under assumption that droplets are distributed according the gamma law against the profile obtained by averaging all estimated reflectivity values shown in Fig. 4.8b and b) comparison between LWC-RRF and simulated EarthCARE RRF.

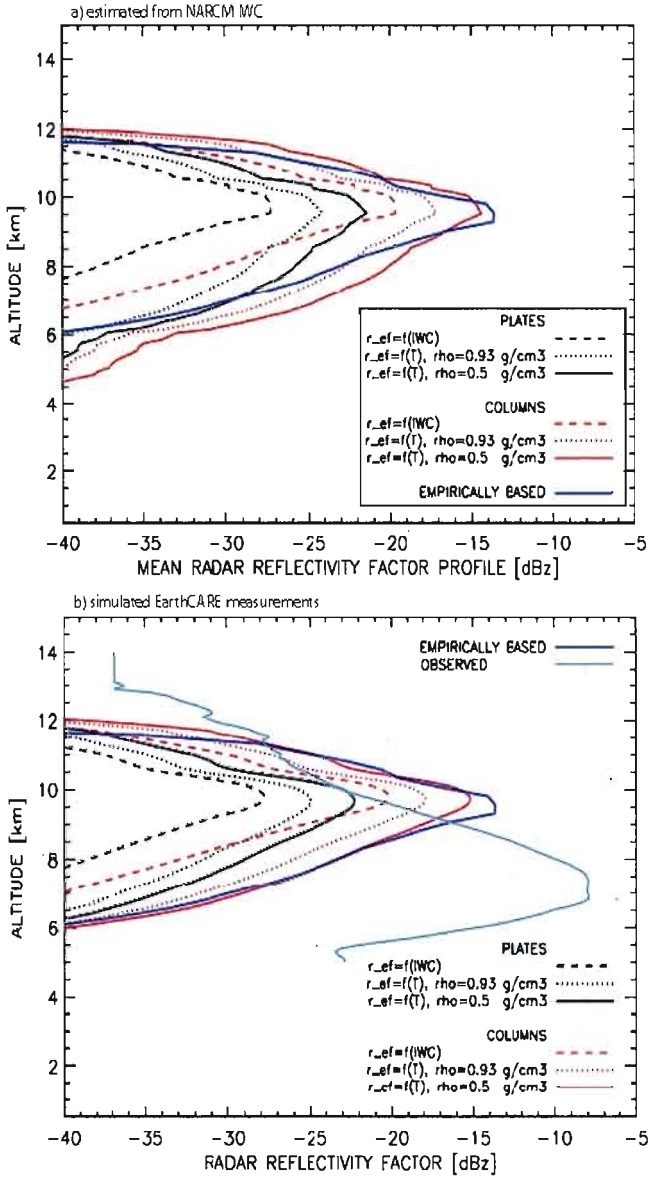

Figure 4.10 Mean vertical profiles of radar reflectivity assuming only solid phase present a) IWC-RRF computed under assumption that ice is distributed according the gamma law and supposing their different shape and density against the profile obtained by averaging of all estimated reflectivity values shown on Fig. 4.8a and b) comparison between IWC-RRF, simulated EathCARE RRF and observed radar reflectivity.

It can be seen in Fig. 4.10a that, according to radar reflectivity, the base of cloud determined by assuming the solid ice density and that the effective radius is expressed as a function of IWC (Lohmann and Roeckner, 1996) is located at higher altitudes than the base of the empirical cloud. Also, the RRF values resulting from Lohmann and Roeckner (1996) parameterisation (dashed black and red lines) are smaller than the averages determined from empirical estimations (blue line). Their RRF maxima differ for about 7 *dBZ* (14 *dBZ*) when cloud ice has the structure of columns (plates). Thus, it follows that the Lohmann and Roeckner (1996) parameterisation does not produce enough large ice in the lower part of cloud (see Fig. 4.7a) as well as in the region with the maximal empirical IWC-RRF values.

As seen in Fig. 4.10a, there is a significant similarity between the empirical IWC-RRF and the IWC-RRF profiles determined by assuming the columns ice crystal shape and the effective radius expressed as a function of the temperature (Lohmann, 2002) (red dotted and full lines). This similarity is remarkable in the case of low-density columns. However, the base of this cloud (red full line, Fig. 4.10a) is located at an altitude lower by 2 *km* against the case of the "empirical" cloud. Also, the IWC-RRF values in the lower part of cloud are larger than those of the empirical IWC-RRF.

The EarthCARE radar measurements are simulated over the ice cloud characterised by identical assumptions with respect to its microphysical properties (effective radius, type and ice bulk density) as in Fig. 4.10a. Their corresponding mean vertical profiles are computed using Equation (27). These simulated profiles, labelled as EC-IWC-RRF are shown in Fig. 4.10b. Also shown in Fig. 4.10b are the empirical profile of radar reflectivity (the same as in Fig. 4.10a) and the mean observed RRF profile (cyan line) from the APEX measurements.

As seen in Fig. 4.10b, there is an excellent agreement between different IWC-RRF profiles and their corresponding EC-IWC-RRF profiles near the top and centre of ice cloud, but less so around cloud base. The base of EarthCARE simulated cloud, in any specific case of microphysical conditions, is located at a little higher altitude than it was the case in Fig. 4.10a. This effect is due to the attenuation of the radar signal in the upper cloud layers. Also, it causes that the EC-IWC-RRF profile in the case of low-density columns and the effective radius parameterized in a function of the temperature, is almost identical to the empirical IWC-RRF profile.

However, as seen in Fig. 4.10b, observed RRF profile completely differs from all simulated profiles. The base of the observed cloud is located at 6 *km* altitude with radar reflectivity values between –20 and –25 *dBZ*. The top of observed cloud reaches reflectivity values of –35 *dBZ* and is located at 13 *km*. The maxima of observed reflectivity are located over the base of cloud at about 7-8 *km* and achieve values between –5 and –10 *dBZ*. In the case of EC-IWC-RRF profiles, maximal RRF values vary from –28 to –15 *dBZ* depending of the assumptions in simulation and are located below 10 *km*. A comparison between simulated and observed RRF values in the base of observed cloud suggests that simulated cloud is located at higher altitude than in the case of observed cloud. Simulated cloud is thinner than observed and the maximal reflectivity values are in the best case for about 5-10 *dBZ* smaller than those of the observed cloud. The distinction between the empirically based and observed reflectivity indicates that there is a lack in ice water content in the NARCM simulation.

The vertical profiles of mean lidar backscattering coefficient calculated from the EarthCARE IS under various assumptions made about the microphysical properties of ice particles are shown in Fig. 4.11. These assumptions are identical to those illustrated in Fig. 4.10b (and also in Fig. 4.10a). All backscattering profiles are obtained under the assumption that the cloud consists only of ice particles. Also shown in Fig. 4.11 is the mean vertical profile of observed backscatter during APEX-E3 (cyan line). It can be seen that there is a considerable similarity between the observed and simulated backscatter profiles between 7 and 11 *km*. However, observed backscattering coefficient is significantly larger than any of simulated profiles below 6 *km* and above 11 *km*, likely indicating that at these altitudes there is more ice particles (and hence IWC) than it is present in NARCM simulation (see Fig. 4.1a) and that the NARCM IWC is underestimated. As the lidar backscatter is approximately proportional to the second power of particle size, it follows that is more sensitive to smaller cloud particles than radar. If the presence of water droplets is included, values of the backscatter coefficient are larger than those observed by several orders of magnitude (not shown), suggesting that NARCM liquid water content may be overestimated at all altitudes. The inferences that the NARCM simulated liquid (ice) water content is likely overestimated (underestimated) are consistent with discussion in Section 4.1.

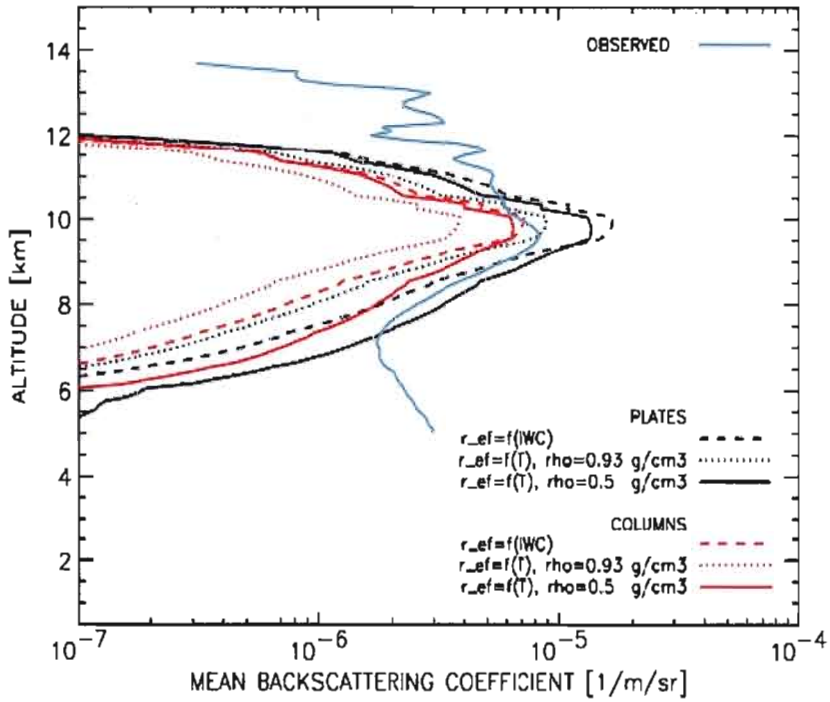

Figure 4.11 Mean backscattering coefficient profiles obtained under various assumptions of shape and composition of ice particles.

4.5 Relative frequency distribution of radar reflectivity and ice water retrieval

Relative frequency (RF) distributions of the corresponding estimated, simulated and observed values of radar reflectivity are shown in Fig. 4.12. The *x*-axis represents radar reflectivity between –45 and 10 *dBZ* divided into intervals of 5 *dBZ*, while the *y*-axis represents the relative frequency of radar reflectivity. Relative frequency distribution of RRF shows the relative frequency of estimated, simulated and observed reflectivity in each of non-overlapping equal RRF intervals of 5 *dBZ* and is represented by the values in the mid-points of each interval. Note that the integral of relative frequencies for each plotted reflectivity is equal 1, so their relative frequency distributions show how the observed, simulated and estimated RRF values are distributed across the reflectivity intervals. Also note that RF

distribution takes into account all observed as well as simulated and estimated RRF values, instead of their corresponding mean profiles, which were discussed in Section 4.4.

In Fig. 4.12, the RF distributions compare the simulated and observed reflectivity for different assumed cloud phases: mixed phase (Fig. 4.12a), ice phase (Fig. 4.12b) and water phase (Fig. 4.12c).

The RF distributions of the estimated and simulated RRFs in Figs. 4.12a and 4.12b refer to the case in which the ice cloud is assumed to be composed of columns, with bulk density of 0.5 gcm^{-3} and with the effective radius determined from Equation 18 (Lohmann, 2002). This case is chosen to further analyse similarities between the mean profile of EarthCARE simulated reflectivity and that computed via empirical IWC-RRF formulas (Fig. 4.10b) against observations during APEX-E3. Estimated reflectivity values refer to those obtained from the NARCM water content assuming that cloud particles are distributed according the modified-gamma distribution and using Equations (29) and (30).

While the simulated EarthCARE radar measurements represent the real measurements of an atmospheric feature involving the limits of the detection method, the estimated RRF represents true evaluations of these measurements. Thus, by comparing the RF distributions of estimated and simulated RRF (black and red lines in Figs. 4.12a, 4.12b and 4.12c), one can see the radar detection limits when observing the microphysical properties of clouds. In the case of a perfect instrument and a perfect detection method, it can be expected that the RF distributions of the estimated and simulated RRF are identical. The attenuation process will move the peak of the RF distribution of simulated RRF toward the lower RRF. This effect can be easily seen in the case liquid cloud (Fig. 4.12c), and is expected as cloud water significantly attenuates the radar signal. Here, the RF distribution peak of simulated RRF is moved into a region between –35 and –40 *dBZ*, and hence, below the EarthCARE detection limit (–35 *dBZ*). This effect produced that the liquid cloud wasn't detected in the mean vertical profile of the simulated EarthCARE radar measurements shown in Fig. 4.9b.

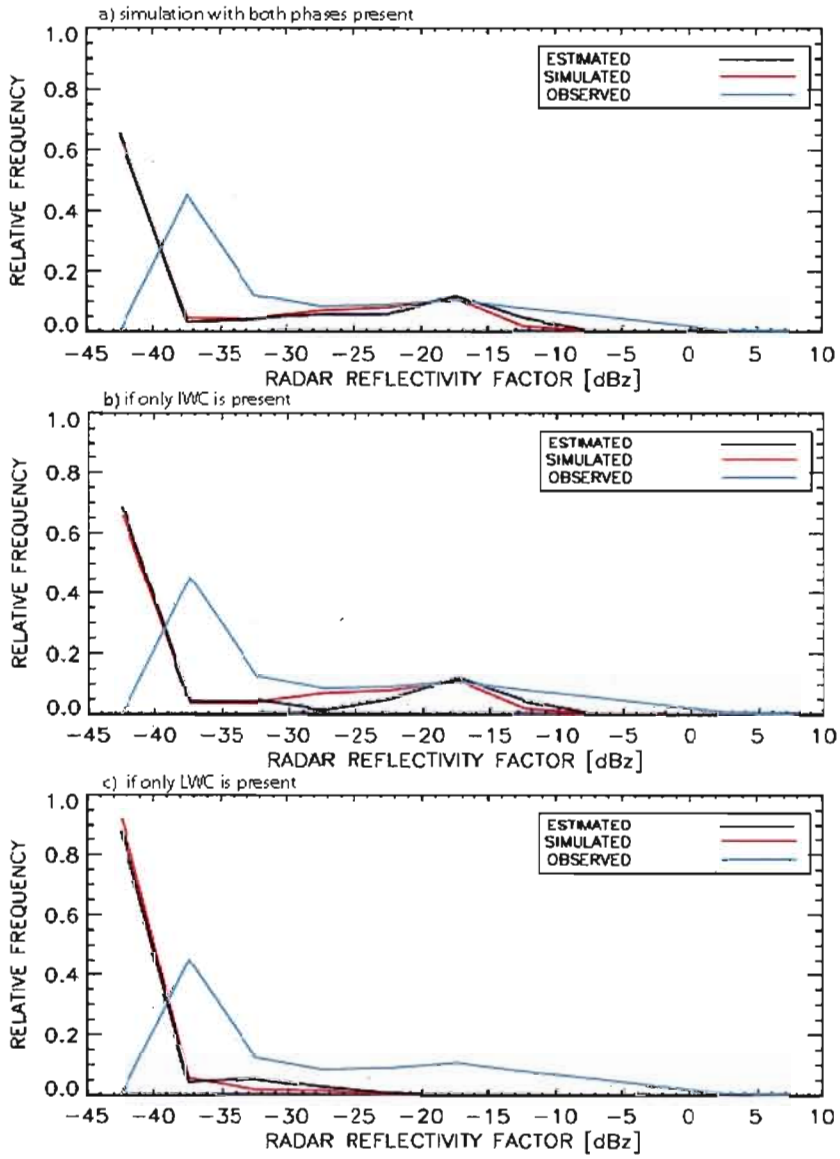

Figure 4.12 a) Relative frequency distribution of estimated, simulated and observed radar reflectivity factor assuming that ice cloud is composed of columns with ice density of 0.5 g/cm^3 and the effective radius determined from Equation 18 (Lohmann, 2002) b) the same as a) but only if solid phase is present and c) as b) but if only liquid phase is present.

As seen in Fig. 4.12b, the attenuation of radar signal due to cloud ice is of small importance as the RF distribution peaks of both estimated and simulated RRF are located in the interval between –15 and –20 *dBZ*. Of more importance is a region between -20 and –30 *dBZ* in which the RF of simulated reflectivity is larger than that of estimated RRF. These large values are produced averaging the cloud masses over the instrument footprints in order to represent the beam filter effect (the IS Radar Beam Filter Effect Module).

It should be expected that the simulated radar signal would be diminished due to attenuation by the existing water in the mixed phase cloud. But, as seen in Figs. 4.12a and 4.12b, the RF distributions of simulated RRF are identical for the mixed phase and the ice phase clouds, although their corresponding RF distributions of estimated RRF differ. This suggests that the EarthCARE IS doesn't treat correctly the mixed phase cloud.

Relative frequency distribution of the observed reflectivity is also shown in Figs. 4.12a, 4.12b and 4.12c (blue line). Note that the minimum detectable level of the APEX-E3 radar was –40 *dBZ*. As seen in these figures, 45 % of the observed reflectivity have values between –35 and –40 *dBZ*, around 15 % reach values higher than –10 *dBZ*, while 40 % of the observed RRF is approximately equally distributed over the range between –35 and –10 *dBZ*. The high frequency of the observed reflectivity between –35 and –40 *dBZ* is most likely caused by variability in cloud conditions over a large area during several hours of the successive radar measurements. The frequencies of observed RRF belonging to the higher limits of reflectivity spectrum are related to the occurrence of maximal RRF values at altitudes around 7 *km* (see the observed RRF profile in Fig. 4.10).

As seen in these figures, the RF distribution of observed RRF covers a broader range than that of estimated (and thus simulated) reflectivity values. The observed reflectivity achieves values of 5 *dBZ* while the maximum of simulated RRF is below –5 *dBZ*. However, the differences in the RF distributions between observed and simulated RRF are expectable in the lower and higher limits of reflectivity spectrum as the extreme local events are hardly simulated by regional model. Of significant importance is the domain between –30 and –5 *dBZ* where the RF distributions of simulated and observed RRF tend to be similar. The presence of their peaks in the same reflectivity level indicates that simulated RRF are, in average, similar to those observed. This was confirmed by comparing the mean vertical RRF

profiles corresponding to these distributions, shown in Fig. 4.10b (cyan and red full line), in spite of dissimilarities in their vertical locations (simulated cloud is located in altitudes higher than in the case of observed cloud).

However, let us recall that the EarthCARE simulated reflectivity between -20 and –30 *dBZ* were produced in order to account for the beam filter effect. In these reflectivity regions, the relative frequencies of observed and simulated reflectivity are similar (Fig. 4.12b). This effect, although present in the APEX-E3 observed reflectivity, is less significant than in the case of the EarthCARE simulated measurements because of differences in the samples volumes of two instruments (the FOV of space-borne radar is larger than in the case of airborne radar), and cannot be easily estimated. So, it should be expected that the relative frequencies of simulated reflectivity would be higher than those of observed reflectivity in this domain. As this effect does not occur, it follows that the relative frequencies of estimated RRF should be higher than they are in the reflectivity range between -20 and –30 *dBZ*. Also seen in Fig. 4.12b is that, in domain between –15 and –5 *dBZ*, the relative frequencies of estimated and simulated reflectivity are lower than in the case of observed RRF.

The differences in the relative frequencies of estimated RRF and observed RRF in the region between –30 and –5 *dBZ* in Fig. 4.12b can only be caused by not enough large NARCM simulated ice water content.

Fig. 4.13 shows the mean vertical profiles of the NARCM simulated ice water content and the ice water retrieved from the observed reflectivity by using the empirical formula of Matrosov (2002) (Fig. 4.8a; Table 4.3). As seen in this figure, the NARCM IWC and the retrieved IWC considerably differ: the NARCM ice water is smaller than retrieved in all altitudes, and also, the altitude where the NARCM IWC reaches maximum is located higher than in the case of the retrieved IWC. Furthermore, at altitudes between 6.5 and 9 *km*, retrieved IWC values are larger even than the maxima in the NARCM IWC.

A comparison between the NARCM IWC and retrieved IWC approves the previously indicated hypothesis that the NARCM simulated IWC is underestimated at almost all altitudes.

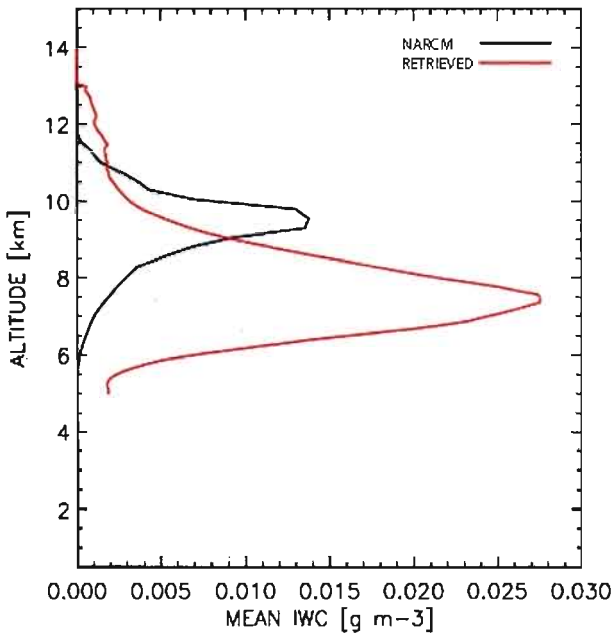

Figure 4.13 Comparison between the NARCM-simulated ice water content (black line) and retrieved ice water content computed using the Matrosov's formula (2002).

4.6 Simulated lidar aerosol returns

The size and mass distributions of aerosol are analyzed in Chapter 4.2. On March 27, 2003, high concentration of sulphates and organic were observed at altitudes up to 3 *km*. Lidar observation of aerosol vertical distribution in the lower atmosphere were not available during this study and that is why the analysis in this subchapter is related only to simulated lidar returns. The aim of the following discussion is to emphasize the significance of the suggested " forward validation method " in the interpretation of the aerosol characteristics from the lidar signal.

The vertical profiles of the mean relative power from the lidar specific observation channels are presented in Fig. 4.14 in the cases of the cloudy and aerosol-free atmosphere

(left) and the atmosphere with both cloud and aerosol present (right). Vertical profiles show high concentration of cloud particles in the layer above 6 km with the maximum located at around 10 km. A relatively strong signal noise in the lower troposphere makes the aerosol detection complex and difficult.

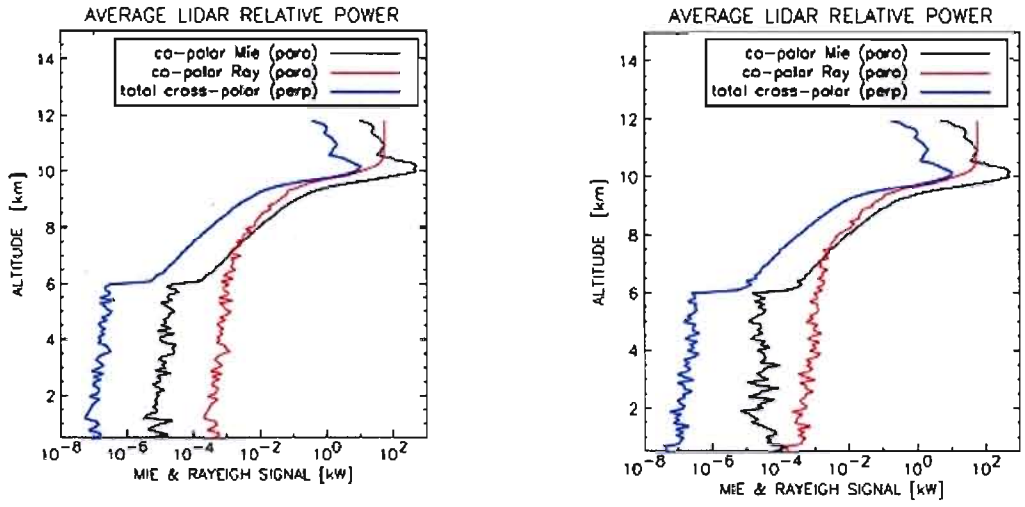

Figure 4.14 Vertical profiles of the mean relative power from the lidar specific observation channels in the case of the cloudy and aerosol-free atmosphere (left) and the atmosphere with both cloud and aerosol present (right).

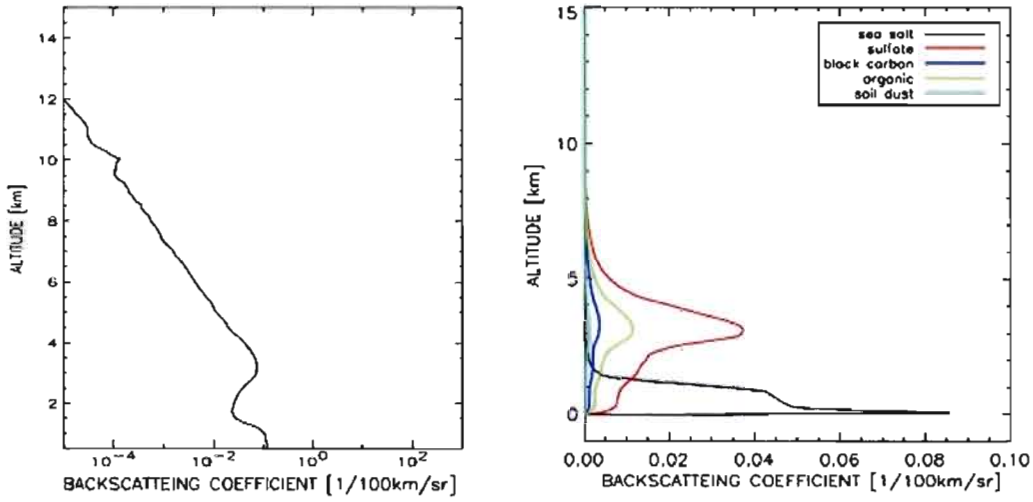

Figure 4.15 Mean vertical profile of the composite aerosol backscattering coefficient in cloud-free atmosphere (left) and the mean vertical backscattering profiles of aerosol components (right).

The mean vertical profile of the aerosol backscattering coefficient the cloud-free atmosphere is shown in Fig. 4.15 (left) along with the corresponding backscattering profiles of aerosol components (right). Vertical profile of a composite aerosol shows high aerosol concentration in the surface layer and subsequent gradual decrease with height. Two local maxima are centred at around 3 *km* and 10 *km*. The lower maximum is located in the layer where the average total aerosol mass concentration reaches its maximum (Fig. 4.3) and is mainly contributed of sulphate and organic aerosol (Figs. 4.15 right and 4.3).

Here, the knowledge of aerosol vertical distribution and composition provides essential information allowing the interpretation of the lidar aerosol return. As the concentration and composition of atmospheric aerosol is highly variable, the employing of the ''forward validation method'' could significantly improve our knowledge about atmospheric physics.

CHAPTER V

SUMMARY AND CONCLUSION

Validation of atmospheric model by space-borne retrieval products introduces uncertainties associated with the retrieval of the microphysical properties of aerosol and clouds. Each retrieval approach assumes some information about shape, size distribution or composition, which can significantly impact retrieved microphysical properties. On the other hand, model simulations can consider explicitly the fundamental physical and cloud (aerosol) microphysical processes. Another way to validate atmospheric model is to apply the forward approach in which an atmospheric model provides the atmospheric state, cloud and aerosol microphysical properties, which are used to simulate the remote-sensing measurements.

In this study, the EarthCARE Instrument Simulator is used as the forward model simulating measurements of space-borne radar and lidar on an atmosphere generated by the NARCM model. In the absence of the space-borne EarthCARE measurements, this method is demonstrated using the APEX-E3 observations. The prime motivation of this research was to explore a general method of validating aerosol and cloud parameterizations in climate models.

The period investigated corresponds to a meteorological situation of the typical advection of air masses from China and Korea with high aerosol concentration. The observation periods from March 25-27 and April 4-7 2003 were reported without dust event but characterized with a strong sulphate loading from anthropogenic origin. On March 27, 2003, high concentration of sulphates and organics (25 and 15 μgm^{-3}, respectively) were observed at altitudes between 1 and 3 *km*. It was found that NARCM aerosol mass concentrations were consistent with observations: simulated aerosol layer was located up to 5 *km* altitude with maximal concentrations at 3 *km*. Sulphates and organic carbon were the most important aerosol components with average concentrations of 5 and 1 μgm^{-3}, respectively, at 3 *km*. However, their maximal concentrations were higher than average observed values by one order of magnitude. Concentrations of simulated dust were remarkably low.

In addition, the size and mass distributions of aerosol were analysed. Results showed that dominant modes of sulphate were located in the 0.1 – 5 μm range indicating that the sulphate size distribution were mostly in the accumulation mode. Distributions of organic and black carbon were low and tended to be present in the larger size range around 1 μm. These results are consistent with observations: observed sulphate distribution were in the accumulation mode, mostly in the 0.4 – 0.7 μm range. Shapes of the observed distributions of other aerosol components were similar to sulphate, but with significantly lower mass concentrations.

The airborne observations reported deep cirrostratus between about 5-6 *km* and 12 *km*. The analyses of the performed simulation confirmed that simulated cloud system for March 27, 2003 matched observed cirrostratus. Simulated mean profiles of IWC and LWC showed a deep cloud of ice layer between about 10 and 12 *km*, mixed phase between 6 and 10 *km* and liquid water between 5 and 6 *km*.

The bulk NARCM liquid and ice water content was approximated by modified-gamma size-distributions of the equivalent radius. With ice phase, two experiments were performed. In the first experiment, the ice effective radius was expressed as a function of IWC (Lohmann and Roeckner, 1996) while in second, as a function of the temperature (Lohmann, 2002). In the first of these methods the effective radius was parameterized according to an empirical relationship between the effective radius of an ice crystal distribution and the observed ice water in frontal clouds, while in the second, as a function of the temperature based on the observations of mid-latitude cirrus.

It was shown that the two ice effective radius parameterizations influenced a considerable difference in total number distributions of ice particles: while the using the frontal clouds parameterisation was characterised with large number of small ice, the parameterization based on the cirrus temperature caused occurring small concentrations of large ice. Furthermore, it was shown that fluctuations of bulk density had a considerable influence: a decrease of ice density was followed by an increase in ice number concentration.

Our estimations of the RRF based on the assumption of the modified-gamma number distribution of the cloud particles were verified by using the empirical relations between ice (liquid) water content and radar reflectivity. Results showed that empirically estimated IWC-

RRF was closest to the RRF-profile acquired by assuming low-density columns whose effective radius was expressed as a function of temperature. In the other hand, results showed discrepancies between the empirical IWC-RRF profile and those RRF profiles whose effective radius was parameterized according to Lohmann and Roeckner (1996). Therefore, it was found that the Lohmann and Roeckner (1996) parameterisation did not produce enough large ice to attain the reflectivity values close to those of estimated IWC-RRF.

The microphysical properties of the NARCM simulated cloud system were converted into radar reflectivity factor and lidar backscattering by using the EarthCARE Instrument Simulator and compared with APEX-E3 airborne radar and lidar measurements. Simulated EC-LWC-RRF values occurred barely at about 9 *km* with a magnitude of about -40 *dBZ*, thus below the EC radar maximal detectable level of -35 *dBZ*. Therefore, simulated EarthCARE radar measurements did not detect the water cloud.

It was found that observed RRF profile completely differed from all simulated profiles. The observed cloud was located at altitudes between 6 and 13 *km* with the maxima between –5 and –10 *dBZ* located over the base of cloud. In the case of EC-IWC-RRF profiles, maximal RRF values varied from –28 to –15 *dBZ* depending of assumptions used in simulations, and were located below 10 *km*, at altitudes where the maximum in ice water content occurred. A comparison between simulated and observed RRF values at the base of observed cloud suggested that simulated cloud was located at higher altitudes compared to observed cloud. Simulated cloud was thinner than observed and the maximal reflectivity values underestimated observations by 5-10 *dBZ*. Furthermore, the fact that the observed and empirically based reflectivity profiles were distinct indicated that there was a lack in amount of ice water content in the NARCM simulation.

Backscattering profiles were achieved under the assumption that the cloud consisted only of ice particles. It was found that observed backscattering coefficient was significantly larger than any of simulated profiles at vertical levels below the base and above the top of observed cloud. This indicated that, at these altitudes, observed ice water content was larger than the NARCM IWC. If the presence of water droplets was included, values of the simulated backscatter coefficient would overestimate observed ones by several orders of

magnitude, suggesting that the NARCM liquid water content could be overestimated at all altitudes where the observed cloud was present.

The RF distribution of observed RRF covered a broader range and was higher than one of estimated (and thus simulated) reflectivity values. It was found that the reflectivity range between–30 and –5 *dBZ* was suitable for the comparison between regional model simulations and APEX-E3 observation. The analyses showed that the differences in the relative frequencies of estimated and observed RRF in this reflectivity region were caused by not enough large NARCM-simulated ice water content.

In the summary, the analyses showed that the Lohmann (Lohmann and Roeckner, 1996) microphysical scheme did not have the ability to produce an amount of ice content in the case of observed cirrostratus. It was found that NARCM underestimated ice water content while likely overestimated liquid water content. The NARCM temperature appeared to be somewhat warmer than observed one at all altitudes and likely partly responsible for the evolving NARCM cloud water content. Meanwhile, an increase in sulphate loading as well as an addition of anthropogenic aerosol might have influenced mixed-phase clouds and thus enhanced the formation of the observed ice cloud system. The Lohmann parameterization (1996) does not account for aerosol chemical composition and assumes that only sulphate acts like CCN. Further, the heterogeneous immersion freezing process is not parameterized in NARCM. All these factors are likely to be responsible for the underestimation of ice water content.

In this study we have applied a "forward" validation method in which the NARCM simulated cloud system is converted into radar reflectivity and lidar backscatter by using the EarthCARE IS. These simulated measurements are compared against the APEX-E3 radar and lidar observations. The results confirm that the applied "forward approach" has a great potential for validation of aerosol and cloud parameterization in climate models. Testing the method, this study leads to its application in more extensive diagnostic for verifications for all clouds and aerosol types against a corresponding real atmosphere. In this sense, further attempts are needed in order to accomplish the validation process.

APPENDIX A

COPIES OF FLIGHT REPORTS FOR MARCH 27th 2003

A1 APEX aircraft report for March 27th 2003[1]

Flight Plan: We are going to fly today with G-II and B200 just in front of the cold front. We will have an ECAV (cloud microphysics measurement) near Koshiki-jima (A: 32:00N, 129.20E; B: 31.35N, 129.20E) in 10:00-12:00, for the condition in front of the cold front. Middle clouds are target.

Flight Report: G-II and B200 flew today (27th) between (A: 32:00N, 129.20E; B: 31.35N, 129.20E) in 10:00-12:00. Being in front of the cold front, we had a cirro-stratus cloud deck with about 5 to 6 km bottom and 12 km top height. Successful flight with five G-II legs; B200 legs at 23,500 ft, 22,500 ft, 21,500 ft, 20,500ft, and 19,500ft. Getting ice crystal particle information. But there is some problem in gust probe and CAPS probe. We are investigating the effect of this problem to the data retrieval.

A2 Daily Briefing Page Rapport[2]

Recommendation:

27 March: There will be rain afternoon, maybe earlier at Fukue. Flight may be difficult. However, it is possible to observe the low cloud between Kagoshima and Amami in the morning, say, 10:00 to 12:00.

Fight menu: Fair weather cloud, depend on local weather and upper cloud condition

28 March: consider a clear sky observation.

Analysis:

Today (27 March)

Weather: The low pressure with cold front moves eastward. The weather will turn to bad with rain and thunder.

Fukue: Cloudy. start to rain from noon.

Amami: Cloudy. Start to rain from afternoon.

Amami-group report: It is fine. FM-CW data has not detected the cloud. The cloud coverage is 6/8. The wind from SW. Wind speed is about 3.1 m/s. SO2 is about 0.4ppb, O3 is 70ppb.

GMS: Cirrus over Fukuejima region. Shallow cumulus around Kagoshima and Amami region.

---

[1] Source: http://157.82.240.167/duckbill/apex/APEX-E3/airobs5.php

[2] Source: http://157.82.240.167/duckbill/apex/APEX-E3/apex04.php#0327

Model: No dust.

Sulfate plume center is over Kyushu, concentration over East China Sea is lower than yesterday.

High BC concentration move eastward with the low pressure.

Satellite overpass: 27th

Terra-> 10:54 JST, Kagoshima, Fair (Amami is located on the "non-sun-glint" side)

TRMM ->09:03 JST, Kagoshima, Fair

SeaStar -> 13:17 JST, Kagoshima, Poor

NOAA16-> 14:25 JST, Kagoshima, Poor

NOAA17-> 10:55 JST, Kagoshima, Good

(Note: Good->Fair->Poor)

March 28, 2003

Yesterday (27 March) analysis:

Flight: G-II and B200 flew (27th) between (A: 32:00N, 129.20E; B: 31.35N, 129.20E) in 10:00-12:00. Being in front of the cold front, we had a cirro-stratus cloud deck with about 5 to 6 km bottom and 12 km top height. Successful flight with five G-II legs; B200 legs at 23,500 ft, 22,500 ft, 21,500 ft, 20,500ft, and 19,500ft. Getting ice crystal particle information. But there is some problem in gust probe and CAPS probe. MODIS & SeaWiFs aerosols: No data for yesterday around experiment area. MODIS clouds: The Terra orbit datafile had troubles (the Terra radiance datafile seemed OK). So, no retrieval has been done. Fukuejima Sky view: thin clouds until 10 o'clock, then heavily overcast; after 13 o'clock, turn to broken; clear after 18 o'clock. Fukuejima Lidar: 3/26, high cloud bases about 8 km in night time. Fukuejima particle counter: Number concentration decreased (esp. after the rain) to 100/cc. AirMass : All component decreased, at least to noon, to about half of yestedays level. Fukuoka: Aerosol number concentration decreased during the morning, to the minimum before 17 o'clock (about 60/cc), then increased. Amami Sky view: fair weather clouds or clear sky until 15:30 when cumulonimbus formed. Amami cloud radar: no available data yet for yesterday, except for early morning. Amami lidar: 3/26, clear sky, occasional cloud base around 1 km. Amami OPC & SSA: SSA from 0.75 to 0.9, minimum at noon. OPC increased after 11 o'clock to above 300/cc, decreased in the night. Amami Gases: O3 between 0.04 and 0.09 ppm. SO2 less than 1 ppb. KCCAR: A thin dust cloud was seen on satellite image approaching Kyushu after the rain cloud.

REFERENCES

Alvarez, R. J. II, L. M. Caldwell, P. G. Wolyn, D. A. Krueger, T. B. McKee and C. Y. She, 1993: Profiling temperature, pressure, and aerosol properties using a high spectral resolution lidar employing atomic blocking filters. *J. Atmos. and Oceanic Techn.*, **V10**, 546-556.

Andronache, C., L. J. Donner, C. J. Seman, C. Ramaswamy and R. S. Hemler, 1999: Atmospheric sulphur and deep convective clouds in tropical Pacific: A model study. *J. Geophys. Res.*, **104**, 4005-4024.

Atlas, D., 1954: The estimation of cloud parameters by radar. *J. Meteor.*, **11**, 309-317.

Atlas, D., S. Y. Matrosov, A. J. Heymsfield, M. –D. Chou and D. B. Wolf, 1995: Radar and radiation properties of ice clouds. *J. Appl. Meteorol.*, **34**, 2329-2345.

Ayash, T., S.L. Gong, C.Q. Jia, P. Huang, T.L. Zhao and D. Lavoue, 2008: Global modelling of multicomponent aerosol species: Aerosol optical parameters. *J. Geophys. Res.*, **113**, D12203, doi: 10.1029/2007JD008968.

Aydin, K. and C. Tang, 1997: Relationships between IWC and polarimetric radar measurements at 94 and 220 GHz for hexagonal columns and plates. *J. Atmos. and Oceanic Techn.*, **14**, 1055-1063.

Bahreini, R., J. L. Jimenez, J. Wang, R. C. Flagan, J. H. Seinfeld, J. T. Jayne, and D. R. Worsnop, 2003. Aircraft-based aerosol size and composition measurements during ACE-Asia using an Aerodyne aerosol mass spectrometer. *J. Geophys. Res.*, **108**, 8645, doi: 10.1029/2002JD003226.

Boucher, O. and U. Lohmann, 1995: The sulfate-CCN-cloud albedo effect. A sensitivity study with two general circulation models. *Tellus*, 47B: 281-300.

Brown, P. R. A., A. J. Illingworth, A. J. Heymsfield, G. M. Mcfarquhar, K. A. Browning and M. Gosset, 1995: The role of space-borne millimeter-wave radar in global monitoring of ice-cloud. *J. Appl. Meteorol.*, **34**, 2346-2366.

Caya, D. and R. Laprise, 1999: A semi-Largrangian semi-implicit regional climate model: The Canadian RCM. *Mon. Weather Rev.*, **127**, 314-362.

Chin, M., D. J. Jacob, G. M. Gardner and P. A. Spiro, 1996: A global three-dimensional model of tropospheric sulfate. *J. Geophys. Res.*, **101**, 18, 667-18, 690.

Comstock, J.M., T.P. Ackerman and G.G. Mace, 2002: Ground-based lidar and radar remote sensing of tropical cirrus clouds at Nauru Island: Cloud statistics and radiative impacts. *J. Geophys. Res.*, **107**, 4714, doi: 10.1029/2002JD002203.

Davis, C. P., K.F. Evans, S.A. Buehler, D.L. Wu and H.C. Pumphrey, 2007: 3-D polarised simulations of space-borne passive mm/sum-mm midlatitude cirrus observations: a case study. *Atmos. Chem. Phys*, 7, 4149-4158.

Donovan, D. P., N. Schutgens, G-J Zadelhov, J.-P. V. Baptista, H. Barker, J.-P. Blanchet, A. Belaulne, W. Symeyer, M. Quante, I. Schimmer, A. Macke, J. Testud, C. Tinel, S. Kato, J. Cole, 2004: The EarthCARE Simulator. Users Guide and Final Report. ESTEC Contract: 15346/01/NL/MM.

Evans, K. F. and G. L. Stephens, 1995: Microwave radiative transfer through clouds composed of realistically shaped ice crystals. Part II: Remote sensing of ice clouds. *J. Atmos. Sci.*, **52**, 2058-2072.

Evans, K. F., S. J. Walter, A. J. Heymsfield and M. N. Deeter, 1998: Modelling of sub-millimeter passive remote sensing of cirrus clouds. *J. Appl. Meteorol.*, **37**, 184-205.

European Space Agency (ESA), 2001: EarthCARE–Earth Clouds Aerosol and Radiation Explorer. ESA SP-1257(1)-The five candidate Earth Explorer Core Missions, ESA/ESTEC, Noordwijk, The Netherlands.

European Space Agency (ESA), 2004: EarthCARE–Earth Clouds Aerosol and Radiation Explorer. ESA SP-1279(1)-The six candidate Earth Explorer Missions, ESA/ESTEC, Noordwijk, The Netherlands.

Fernald, F. G., 1984: Analysis of atmospheric lidar observation: Some comments. *Appl. Opt.*, **23(5)**, 652-653.

Fox, N. and J. Illingworth, 1997: The retrieval of stratocumulus cloud properties by ground-based cloud radar. *J. Appl. Meteorol.*, **36**, 485-492.

Franke, K., A. Ansmann, D. Muller, D. Althausen, F. Wagner and R. Scheele, 2001: One-year observations of particle lidar ratio over the tropical Indian Ocean with Raman lidar. *Geophys. Res. Lett.*, **28**, 4559-4562.

Girard, E. and J. –P. Blanchet, 2001: Simulation of Arctic diamond dust, ice fog, and thin stratus using an explicit aerosol-cloud-radiation model. *J. Atmos. Sci.*, **58**, 1199-1221.

Gobby, G. P., F. Barnaba, M. Blumthaler, G. Labow, and J. R. Herman, 2002: Observed effects of particle non-sphericity on the retrieval of marine and desert dust aerosol optical depth by lidar. *Atmos. Res.*, **61**, 1-14.

Gong, S. L., L. A. Barrie and J. –P. Blanchet, 1997: Modelling sea-salt aerosols in the atmosphere: 1. model development. *J. Geophys. Res.*, **102**, 3805-3818.

Gong, S. L., L. A. Barrie, J. -P. Blanchet, K. von Salzen, U. Lohmann, G. Lesins, L. Spacek, L. M. Zhang, E. Girard, H. Lin, R. Leaitch, H. Leighton, P. Chylek and P. Huang, 2003 : CAM: A Size Segregated Simulation of Atmospheric Aerosol Processes for Climate and Air Quality Models. 1. Module Development. *J. Geophys. Res.*, **108**, D1, 4007-4022.

Gorbunov, B., A. Baklanov, N. Kakutkina, H. L. Windsor and R. Toumi, 2001: Ice nucleation on soot particles. *J. Atmos. Sci.*, **32**, 199-215.

Graf, H. –F., J. Feichter and B. Langmann, 1997: Volcanic sulfate emission: Estimates of source strength and its contribution to the global sulfate distribution. *J. Geophys. Res.*, **102**, 10, 727-10, 738.

Grund, C. J. and E. W. Eloranta, 1991: The University of Wisconsin High Spectral Resolution Lidar. *Opt. Eng.*, **30**, 6-12.

Hess, M., P. Koepke, and I. Schult, 1998: Optical Properties of Aerosols and Clouds: The software package OPAC. *Bull. Am. Met. Soc.*, 79, 831-844.

Heymsfield, A. J. and C. M. R. Platt, 1984: A parameterization of the particle size Spectrum of ice clouds in terms of the ambient température and the ice water content. *J. Geophys. Res.*, **41**, 846-855.

Heymsfield, A. J. and G. M. McFarquhar, 2001: Microphysics of INDOEX clean and polluted trade cumulus clouds. *J. Geophys. Res.*, **106**, 28653-28674.

Heymsfield, A. J. and G. M. McFarquhar, 2002: Cirrus, chap. Mid-latitude and tropical cirrus: microphysical properties. Oxford University Press, Inc., New York, 78-101.

Hogan, R. J. and A. J. Illingworth, 1999: The potential of space-borne dual-wavelength radar to make global measurements of cirrus clouds. *J. Atmos. and Oceanic Techn.*, **16**, 518-531.

Hu, R. –M., J. –P. Blanchet and E. Girard, 2005: Evaluation of the direct and indirect radiative and climate effects of aerosols over the western Arctic. *J. Geophys. Res.*, **110**, D11213, doi: 10.1029/2004JD005043.

Hu, Y. X., and K. Stamnes, 1993: An accurate parameterization of the radiative properties of water clouds suitable for use in climate models. *J. Clim.*, **6**, 728-742.

Johnson, D. W., 1993: Parameterisation of the cloud topped boundary layer. Aircraft measurements. In: ECMWF Workshop Proc 'Parameterization of the cloud topped boundary layer', ECMWF, Reading, UK, pp 77-117.

Karyampudi, V. M., S. P. Palm, J. A. Reagen, H. Fang, W. B. Grant, R. M. Hoff, C. Moulin, H. F. Pierce, O. Torres, E. V. Browell and S. H. Melfi, 1999: Validation of the Saharan dust plume conceptual model using lidar, Meteosat and ECMWF data. *Bull. Am. Met. Soc.*, **80**, 1045-1075.

Klett, J. D., 1981: Stable analytical inversion solution for processing lidar return. *Appl. Opt.*, **20**, 211-220.

Klett, J. D., 1985: Lidar inversion with variable backscatter/extinction ratios. *Appl. Opt.*, **24(11)**, 1638-1643.

Knollenberg, R. G., 1970: The Optical array : An alternative to scattering and extinction for airborne particle size détermination measurements. *J. Appl. Meteor.*, **9**, 86-103.

Kovalev, V. A., 1995: Sensitivity of the lidar solution to errors of the aerosol backscatter-to-extinction ratio: Influence of a monotonic change in the aerosol extinction coefficient. *Appl. Opt.*, **34(18)**, 3457-3462.

Laprise, R., D. Kaya, G. Bergeron and M. Giguère, 1997: The formulation of André Robert MC2 (Mesoscale Compressible Community) model. In the André J. Robert Memorial Volume (C. Lin, R. Laprise and H. Ritchie, Eds.). Companion volume to *Atmos.-Ocean*: 195-220.

Lee, C. H., C. B. Park and J. H. Kim, 2004: 532/1064 nm ACA lidar measurements of Asian dust at Suwon, Korea during 2002/spl sim/2004. In Remote Sensing of Atmospheric Aerosols, 2005, IEEE Workshop, 9-13.

Liou K., N., 1992 : Radiation and Cloud Processes in the Atmosphere-Theory, Observation and Modeling. *Oxford University Press*. Oxsford.

Liou K., N, 2002: An Introduction to Atmospheric Radiation, Volume 84, Academic Press, Second Edition by Grant W. Petty.

Liu, C., and A. J. Illingworth, 2000: Toward more accurate retrievals of ice water content from radar measurements of clouds. *J. Appl. Meteor.*, **39**, 1130-1146.

Liu Z., A.H. Omar, Y. Hu, M. A. Vaughan and D. M. Winker, 2005: CALIOP Algorithm Theoretical Basis Document; Part 3: Scene Classification Algorithms, NASA, PC-SCI-202 Part 3.

Lohmann, U. and E. Roeckner, 1996: Design and performance of new cloud micro-physic scheme developed for the ECHAM general circulation model. *Clim. Dyn.*, **12**, 557-572.

Lohmann, U., 2002: Possible aerosol effects on ice clouds via contact nucleation. *J. Geophys. Res.*, **59**, 647-656.

Lohmann U., and J. Feichter, 2005: Global indirect aerosol effects: A Review. *Atmospheric Chemistry and Physics*, **5**, 715-737.

Mace, G. G., T.P. Ackerman, P. Minnis and D. F. Young, 1998: Cirrus layer microphysical properties derived from surface-based millimeter radar and infrared interferometer data. *J. Geophys. Res.*, **103**, 23 207-23 216.

Matrosov, S. Y., R. F. Renking, R. A. Kropfli and B. W. Bartram, 1996: Estimations of ice hydrometeor types and shapes from radar polarization measurements. *J. Atmos. and Ocean Tech.*, **13**, 85-96.

Matrosov, S. A., V. Korolev and A. J. Heymsfield, 2002: Profiling cloud ice mass and particle characteristic size from Doppler radar measurements. *J. Atmos. and Ocean Tech.*, **19**, 1003-1018.

McFarlane, N., A., G. J. Boer, J. -P. Blanchet and M. Lazare, 1992: The Canadian Climate Centre second-generation general circulation model and its equilibrium climate. *J. Clim.*, **5**, 1013-1044.

McGill, M. J., L. Li, W. D. Hart, G. M. Heymsfield, D.L. Hlavka, P. E. Racette, L. Tian, M. A. Vaughan and D. M. Winker, 2004: Combined lidar-radar remote sensing: Initial results from CRYSTAL-FACE. *J. Geophys. Res.*, **109**, D07203.

Moss, S. J. and D. W. Johnson, 1994: Aircraft measurements to validate and improve numerical model parameterizations of ice to water ratios in clouds. *Atmos. Res.*, **34**, 1-25.

Mukai, S., I. Sano and B. N. Holben, 2005: Aerosol properties over Japan determined by sun/sky photometry. *Water, Air and Soil Pollution: Focus*, **5**, 133-143.

Noel, V., D. M. Winker, T. J. Garrett and M. McGill, 2007: Extinction coefficients retrieved in deep tropical ice clouds from lidar observations using a CALIPSO-like algorithm compared to in-situ measurements from the cloud integrating nephelometer during CRYSTAL-FACE. *Atmos. Chem. Phys*, 7**(5)**, 1415-1422.

Ou, S. –C. and K. –N. Liou, 1995: Ice microphysics and climate temperature feedback. *Atmos. Res.*, **35**, 127-138.

Pawlowska, H. and J. –L. Brenguier, 2000: Microphysical properties of stratocumulus clouds during ACE-2. *Tellus*, **52B**, 868-887.

Penner, J. E., R. E. Dickinson and C. A. O'Neil, 1992: effects of aerosol from biomass burning on the global radiation budget. *Science*, **256**, 1432-1433.

Piironen, P. and E. W. Eloranta, 1994: Demonstration of a high-spectral-resolution lidar based on an iodine absorption filter. *Opt. Lett.*, **V19**, 234-236.

Platt, C. M. R., 1981: Remote sensing of High Cloud. III: Monte Carlo Calculations of Multiple-Scattered Lidar Returns. *J. Atmos. Sci.*, **38**, 156-167.

Platt, C. M. R., and Winker, D. M., 1994: Vertical distribution and optical depths of clouds from LITE observations, *Lidar Techniques for Remote Sensing, Proc. SPIE*, **2310**, 106-115.

Pruppacher, H. R. and J. D. Klett, 1978: Microphysics of Cloud and Precipitation. Reidel, Dordrecht.

Robert, A., T. L. Yee and H. Ritchie, 1985: A semi-Lagrangian and semi-implicit numerical integration scheme for multilevel atmospheric models. *Mon. Wea. Rev.*, **113**, 388-394.

Ryzhkov, A. V., D. S. Zrnic and B. A. Gordon, 1998: Polarimetric Method for Ice Water Content Determination. *J. Appl. Meteor.*, **37**, 125-134.

Saleh B. E. A. and M.C. Teich, 1991: Fundamentals of Photonics. Wiley-Interscience, New York.

Sasano, Y., E. V. Browell and S. Ismail, 1985: Error caused by using a constant extinction/backscattering ratio in the lidar solution. *Appl. Opt.*, **24**, 3929-3932.

Sassen, K., 2002: Indirect climate forcing over the western US from the Asian dust storms. *Geophys. Res. Lett.*, **29**, 10, 10.1029/2001GL014051.

Sauvageot, H. and J. Omar,1987: Radar reflectivity of cumulus clouds. *J. Atmos. and Oceanic Techn.*, **4**, 264-272.

Schneider, T. L. and G. L. Stephens, 1995: Theoretical aspects of modelling backscattering by cirrus particles at millimeter wavelengths. *J. Atmos. Sci.*, **52**, 4367-4385.

Seifert, M., J. Ström, R. Krejci, A. Minikin, A. Petzold, J. –F. Gayet, H. Schlager, H. Zierceis, U. Schumann and J. Ovarlez, 2004: Aerosol-cirrus interactions: a number based phenomenon at all?. *Atmos. Chem. Phys.*, **4**, 293-305.

Spacek, L., S. Gong , K. von Salzen , U. Lohmann , P. Liu , R. Vet , C. Ro , J. -P. Blanchet, L. A. Barrie , H. G. Leighton, R. Leaitch, R. M. Hoff , E. Girard, 1999: The NARCM aerosol model applied to eastern North America LITE shuttle measurement period. Unpublished manuscript.

Stephens, G.L., 1994: Remote sensing of the lower atmosphere: an introduction. New York: Oxford University Press.

Stephens, G. L., D. G. Vane, R. J. Boain, G. G. Mace, K. Sassen, Z. Wang, A. J. Illingworth, E. J. O'Connor, W. B. Rossow, S. L. Durden, S. D. Miller, R. T. Austin, A. Benedetti, C. Mitrescu, and CloudSat Science Team, 2002: The CloudSat mission and the A-train: A new dimension of space-based observations of clouds and precipitation. *Bull. Am. Met. Soc.*, **83**, 1771-1790, doi: 10.1175/BAMS-83-12-1771.

Takami, A., T. Miyoshi, A. Shimono and S. Hatakeyama, 2005: Chemical composition of fine aerosol measured by AMS at Fukue Island, Japan during APEX period. *Atmos. Environ.*, **39**, 4913-4924.

Tegen, I., P. Hollrig, C. Chin, I. Fung, J. Daniel and J. Penner, 1997: Contribution of different aerosol species to the global aerosol extinction optical thickness: Estimates from model results. *J. Geophys. Res.*, **102**, 23, 895- 23, 915.

Turner, D. D., 2005: Arctic mixed-phase cloud properties from AERI-lidar observations: Algorithm and results from SHEBA. *J. Appl. Meteor.*, **44**, 427-444.

Ulaby, F. T., R. K. Moore and A. K. Fung, 1981: Microwave remote sensing, active and passive. Artech House. Vol.1.

Vaughan, M., S. Young, D. Winker, K. Powell, A. Omar, Z. Liu, Y. Hu and C. Hostetler, 2004: Fully automated analysis of space-based lidar data: an overview of the CALIPSO retrieval algorithms and data products. *Proc. SPIE*, **5575**, 16-30.

Von Salzen, K., H.G. Leighton, P.A. Ariya, L.A. Barrie, S.L. Gong, J.-P. Blanchet, L. Spacek, U. Lohmann and L. I. Kleinman, 2000 : Sensitivity of sulphate aerosol size distributions and CCN concentrations over North America to SO_x emissions and H_20_2 concentrations. *J. Geophys. Res.*, **105**, n°D8, 9741-9765.

Walko, R. L., W. R. Cotton, M. P. Meyers and J. Y. Harrington, 1995: New RAMS cloud microphysics parameterisation. Part I: The single-moment scheme. *Atmos. Res.*, **38**, 29-62.

Wang, X., A. Boselli, L. D. Avino, R. Velotta, N. Spinelli, P. Bruscaglioni, A. Ismaelli and G. Zaccanti, 2005: An algorithm to determine cirrus properties from analysis of multiple-scattering influence on lidar signal. *Appl. Phys. B.*, **80**, 609-615.

Weng, F. and N. C. Grody, 2000: Retrieval of ice parameters using a microwave imaging radiometer. *J. Atmos. Sci.*, 1069-1081.

Winker, D. M., R. H. Couch and M.P. McCormick, 1996: An overview of LITE: NASA's LidaR In-space Technology Experiment. *Proc. IEEE*, **V84**, 164-180.

Winker, D. M., 1997: Simulation and modelling of multiple scattering effects observed in LITE data, in *Advances in Atmospheric Remote Sensing with Lidar*, A. Ansmann, U. Wandinger, R. Neuber and P. Rairoux, eds., (Springer, New York, 1997), pp. 185-188

Winker, D. M., J. Pelon and M. P. McCormick, 2002: The CALIPSO mission: Space-borne lidar for observation of aerosol and clouds. *Proc. SPIE*, **4893**, 1-11.

Young, S., 1995: Analysis of lidar backscatter profiles in optically thin cirrus. *Appl. Opt.*, **34**, 7019-7031.

Zhang, G. J. and N. A. McFarlane, 1995: Sensitivity of climate simulations to the parameterisation of cumulus convection in the Canadian Climate Centre General Circulation Model. *Atmosphere-Ocean*, **33**, 407-446.